Applied Physics A (2023) 129:807
https://doi.org/10.1007/s00339-023-07079-x

Applied Physics A
Materials Science & Processing

Investigation of the structural, morphological and magnetic properties of barium hexaferrite added with magnesium oxide nanoparticles

Majed Sharrouf[1] · R. Awad[2] · Khulud Habanjar[1]

Received: 12 June 2023 / Accepted: 14 October 2023 / Published online: 31 October 2023

Abstract
$(BaFe_{12}O_{19})_{1-x}/(MgO)_x$ nanocomposites, with weight fraction $x = 0$, 0.1, 0.2, 0.4, 0.8 and 1, have been synthesized by co-precipitation method followed by high-speed ball-milling techniques. Structural, optical, and magnetic properties have been studied. XRD analysis confirmed the formation of the two pure phases $BaFe_{12}O_{19}$ and MgO, with the formation of a $MgFe_2O_4$ as a minor phase in the nanocomposites. Transmission electron microscopy (TEM) followed by high resolution TEM and SAED were used to study the morphology, crystallinity and lattice spacing, respectively. TEM micrographs revealed the co-existence of spherical and nanorod-shaped particles for pure $BaFe_{12}O_{19}$, and cubic shape for MgO nanoparticles. Raman spectrum for $BaFe_{12}O_{18}$ showed strong and sharp modes, identifying the formation of barium hexaferrite phase. However, MgO showed two broad peaks attributed to G and D bands. The energy dispersive X-ray and scanning electron microscope were performed for elemental analysis and surface topography, respectively. The real elemental compositions matched well with the starting values. X-ray photoelectron spectroscopy was conducted for the investigation of the elemental compositions and the oxidation states of (Ba^{2+}, Fe^{2+}, Fe^{3+} Mg^{2+} and O^{2-}). The magnetic properties like saturation magnetization, remanent magnetization, coercivity and squareness ratio have been determined using the *M–H* loops. These loops revealed the hard ferromagnetic behavior of pure barium hexaferrite and the mixture of ferromagnetism with diamagnetic behavior at high fields for pure MgO. The saturation and remanent magnetizations decreased with the addition of MgO phase. d*M*/d*H* curves showed a weak magnetic coupling between the hard magnetic $BaFe_{12}O_{19}$ and the soft magnetic $MgFe_2O_4$.

Keywords $BaFe_{12}O_{19}$ · MgO · Nanocomposites · SAED · Ferromagnetic

1 Introduction

In the past few years, the investigation of magnetic nanoparticles had attracted much attention because of their targets in different technological applications. These include information storage, magnetic recording, magnetic resonance imaging and catalyst [1, 2]. Hexagonal ferrites, with general formula of $MFe_{12}O_{19}$ (M is a divalent metal), have gained much attention as hard magnetic materials. Barium hexaferrite ($BaFe_{12}O_{19}$) is the one of the most promising magnetic nanoparticles. $BaFe_{12}O_{19}$ is specified by its superior properties, with a high Curie temperature, chemically stable, low production cost, corrosion resistivity and high coercively [3, 4]. Among numerous metal oxide nanoparticles, magnesium oxide (MgO) is known by its fascinated mechanical, chemical, and biological properties. It is characterized by an outstanding stability, high surface reactivity, and good biocompatibility. It is considered a suitable semiconductor with a wide bandgap, reflecting the good optical properties, and is a constructive factor for biomedical applications.

For the improvement of different nanoscale materials, adding impurities, changing the manufacturing process, or introducing them into a composite material could be done. Many studies of these composite materials are being proposed by researchers to investigate their structure, magnetism, and optical behavior.

The study of oxide-ferrite nanocomposites has been reported by many researchers [5–8]. The improvement of

✉ Khulud Habanjar
k.habanjar@bau.edu.lb

[1] Department of Physics, Beirut Arab University, Beirut, Lebanon

[2] Department of Physics, Alexandria University, Alexandria, Egypt

magnetic properties was reported in nanocomposites formed of soft/hard magnetic phases. This can be beneficial for developing superior permanent magnets [9–12]. Khan et al. [7] reported the spring exchange coupling of $BaFe_{12}O_{19}$/$NiFe_2O_4$ nanocomposites due to strong magnetic interactions. According to Hoque et al. [8], single-phase permanent magnet behavior may be seen in hard/soft $CoFe_2O_4$/$BaFe_{12}O_{19}$ and $MgFe_2O_4$/$BaFe_{12}O_{19}$ nanocomposites. Also, the structural and magnetic properties of $BaFe_{12}O_{19}$/$NiFe_2O_4$ nanocomposites showed the co-existence of both nanoparticles with well distinguished grains [9], with an enhancement in the saturation magnetization (M_s) compared to non-exchange coupled system. Yang et al. [10] reported an excellent exchange coupling in $(1-x)BaFe_{12}O_{19}/xCoFe_2O_4$ nanocomposites, prepared by the microwave sintering method. MgO was used as an effective candidate for enhancing the properties of different ferrites [11–13]. Ali et al. [12] reported the enhancement of microwaves absorption properties of $CuFe_2O_4$ magnetic nanoparticles embedded in MgO matrix. Also, Li et al. [11] reported the growth inhibition of $MgFe_2O_4$ grains when MgO was added. The particle size decreased with an increase in the specific area as the volume fraction of MgO increases.

Nanoparticles are synthesized by various techniques; Sol–gel auto-combustion, micro-emulsion and hydrothermal technique [14]. Co-precipitation method is generally used due to some advantages: it is a simple, reliable, cost-effective and time-consuming method [15]. Also, the produced nanoparticles are formed by a homogeneous powder with maximum yield and does not require any organic fuels. As for nanocomposites, the ball-milling process is the easiest one. The powdered materials suffer collisions with the grinding media, leading to a homogeneous mixture and allowing a good control over the particles size [16].

Thorough literature survey, there is no detailed study has been carried out on $BaFe_{12}O_{19}$/MgO nanocomposites. Hence, this study highlights the synthesis of $(BaFe_{12}O_{19})_{1-x}/(MgO)_x$ nanocomposites, with $x=0$, 0.1, 0.2, 0.4, 0.8 and 1. $BaFe_{12}O_{19}$, MgO and their nanocomposites have been synthesized via co-precipitation method and ball-milling, respectively. The samples were studied through structural, optical, and magnetic properties.

2 Experimental techniques

The wet chemical co-precipitation method was used to prepare pure MgO and $BaFe_{12}O_{19}$ nanoparticles. $(BaFe_{12}O_{19})_{1-x}/(MgO)_x$ nanocomposites were prepared via high-speed ball milling method, with $x=0.1$, 0.2, 0.4 and 0.8.

For the synthesis of pure $BaFe_{12}O_{19}$ nanoparticles, iron (III) chloride hexahydrate ($FeCl_3{\bullet}6H_2O$), barium chloride dihydrate ($BaCl_2{\bullet}2H_2O$), an alkali solution of 4.0 M sodium hydroxide (NaOH) and deionized water, as dispersing solvent, were used as starting materials. 1 M iron (III) chloride hexahydrate ($FeCl_3{\bullet}6H_2O$) and 1 M barium chloride dihydrate ($BaCl_2{\bullet}2H_2O$) solutions were prepared by dissolving each of iron (III) chloride ($FeCl_3{\bullet}6H_2O$, ≥ 98%, Sigma-Aldrich) and barium chloride ($BaCl_2{\bullet}2H_2O$, ≥ 98%, Sigma-Aldrich) with deionized water. Both solutions were mixed and subjected to continuous magnetic stirring at room temperature. To adjust the solution at highly basic condition (pH 13), a solution of 4 M NaOH was added dropwise to the solution which is convenient for the direct preparation of $BaFe_{12}O_{19}$ crystals. Afterwards the reaction was stirred for 2 h at 80 °C. The resultant precipitate was washed continuously with deionized water to remove the residues, until the pH reached 7 and then dried at 100 °C for 16 h in air.

For the synthesis of MgO nanoparticles, the starting materials used are magnesium chloride ($MgCl_2{\bullet}6H_2O$), an alkali solution of 4.0 M sodium hydroxide (NaOH) and deionized water. 1 M magnesium chloride hexahydrate ($MgCl_2{\bullet}6H_2O$) was prepared by mixing ($MgCl_2{\bullet}6H_2O$, ≥ 99%, Sigma-Aldrich) with deionized water. Then, the obtained solution was stirred continuously at room temperature. A solution of NaOH of 4 M was added dropwise to attain a pH 12. Afterwards the solution was stirred for 6 h at room temperature until a white precipitate was formed. The resultant product was washed with a solution of 50% deionized water and 50% ethanol until the pH decreased to 7. The powder obtained was dried at 80 °C for 12 h in air.

The resultant powder was grinded and divided into 6 parts with the general formula $(BaFe_{12}O_{19})_{1-x}/(MgO)_x$ ($x=0$, 0.1, 0.2, 0.4, 0.8 and 1). For the nanocomposites, different percentages of $BaFe_{12}O_{19}$ and MgO were weighted and then ball milled via PM 100 Planetary Ball Milling machine. The ball to powder weight ratio used is 5:1 at a speed of 300 rpm for 10 min. Finally, the six samples were calcined at 950 °C for 4 h.

XRD patterns were obtained using Bruker D8 advance powered diffractometer with *Cu-k α* radiation ($\lambda=1.5406$ Å) and scan speed 3°/min in the range of $20° \le 2\theta \le 80°$. The shape and the size of the prepared nanoparticles as well as HR-TEM and SAED images were investigated using the JEM 100 CX Transmission Electron microscope (TEM). The images provided magnification from 100× to 250,000× with a resolution of 1 Å, operating at a voltage of 80 kV. The Raman spectra were obtained using Raman spectrometer (Model: SENTERRA, BRUKER OPTICS). The wavelength used is $\lambda=659$ nm and a power of 20 W. The conditions are continuous mode time of 10 s, snapshot time of 7 s, number of accumulations set to 30 time and a microscope objective lens of 100×. EDX spectra and SEM images were obtained at room temperature using JSMIT200 Energy Dispersion X-ray machine. The XPS was collected on K-Alpha

(ThermoFisher Scientific, USA) with monochromatic X-ray *Al-k*α radiation of energy range 10–1350 eV and spot size of 400 µm at pressure 10^{-9} mbar. The pass energy was 200 eV for the full survey XPS spectra, and 50 eV for the high-resolution XPS spectra. The binding energy scale is calibrated using silver (Ag) and gold (Au) standard sheets. The magnetic hysteresis loops were investigated by Lakeshore 7410 VSM. The magnetic field is set to range between − 20,000 G to + 20,000 G, at room temperature.

3 Results and discussion

The phases and the structural parameters of $(BaFe_{12}O_{19})_{1-x}/(MgO)_x$ nanocomposites, with $x = 0$, 0.1, 0.2, 0.4, 0.8 and 1, were investigated via X-ray powder diffraction. XRD patterns along with the corresponding Rietveld refinements are shown in Fig. 1. Clearly, the MAUD refinements of pure $BaFe_{12}O_{19}$ and MgO revealed the formation of the two main phases with high crystallinity and purity; The hexagonal structure of barium hexaferrite and the cubic structure of magnesium oxide were depicted with space group *P6₃/mmc* [17] and Fm $\bar{3}$ m [18], respectively. α-Fe_2O_3 was detected in pure hexaferrite as a minor phase. The same result was reported by Habanjar et al. [19], when studying the effect of calcination temperature and cobalt addition on the structure of barium hexaferrite nanoparticles. For the nanocomposites, the refined XRD patterns confirmed the existence of both $BaFe_{12}O_{19}$ and MgO in one matrix along with the formation of cubic $MgFe_2O_4$ as a secondary phase. Kumar et al. [20] reported the formation of $MgFe_2O_4$ to the calcination temperature and the performed preparation method. Moreover, A study was performed by Azhari et al. [21] about the phase evolution in Fe_2O_3/MgO nanocomposite prepared via simple precipitation method. It was reported that $MgFe_2O_4$ phase was formed at a temperature of 600 °C, and this might be the reason for the disappearance of α-Fe_2O_3 in our nanocomposite samples, as it might have reacted with MgO to form the $MgFe_2O_4$ phase. The refinement progress of experimental XRD pattern is monitored by the goodness of fit (GoF) which is defined as the ratio of the weight residual error (R_{wp}) to the expected residual error (R_{exp}) [22], and their corresponding values are shown as insets in Fig. 1. The values of GoF, which are very close to unity, confirmed the successful formation and incorporation of the nanomaterials with different crystalline structures in the matrices of the formed nanocomposites [23].

The weight percentages of all phases in the different nanocomposites, extracted from MAUD, are plotted in Fig. 2. Obviously, the composition of the considered nanocomposites is verified compared to their starting material percentages. As the content of MgO increases, its weight percentage increases with a decrease in $BaFe_{12}O_{19}$ and formation of $MgFe_2O_4$ contents. This is also confirmed by comparing the calculated atomic percentages of all elements (Ba, Fe, Mg and O) obtained from MAUD software to the theoretical values, as shown in Table 1.

The structural features of $BaFe_{12}O_{19}$, MgO and their nanocomposites were investigated from the extracted microstructural parameters. Lattice parameters and microstrain were extracted from MAUD software and graphed in Fig. 3. The lattice parameters of the hexagonal $BaFe_{12}O_{19}$ ($a = 5.888$ Å and $c = 23.199$ Å) are similar to the results obtained by Alam et al. [24] for the undoped Ba-hexaferrite prepared by co-precipitation method. As shown in Fig. 3a, a and c show a slight change as MgO content increases up to $x = 0.4$. However, at $x = 0.8$, the two lattice parameters changed significantly to 5.914 Å and 23.066 Å with a relatively large decrease in the microstrain. This can be explained by the fact that the stress field from grain boundaries can cause deviations of atoms in the crystallites from their ideal sites [25]. Such an effect is mainly concentrated in a region near the grain boundaries, which not only generates a local lattice strain but also changes the lattice parameters as reported by Qin et al. [25]. However, The ratio c/a lies in the expected range (3.90–3.94) similar to the one reported by Kaur et al. [26]. For the cubic MgO phase, the lattice parameter a decreased with the microstrain from 4.212 Å for $x = 0.1$–4.208 Å for $x = 0.2$, as seen in Fig. 3b. The value of a obtained for $MgFe_2O_4$ phase showed a similar behavior as the two main phases and changed significantly from 8.385 Å ($x = 0.4$) till 8.409 Å ($x = 0.8$) because of the observed large change in the microstrain. The crystallite size (D) was calculated using Debye–Scherrer's equation [27]:

$$D = \frac{0.9\,\lambda}{\beta \cos\theta}, \tag{1}$$

where "2θ" is the diffraction angle and "β" is full width half maxima of the primary peaks. As listed in Table 2, the crystallite size of $BaFe_{12}O_{19}$ is 25.5 nm and it ranges between 21.9 nm and 24.5 nm for $0 < x \leq 0.8$. This is comparable to the values obtained by Vadivelan et al. [28] for $BaFe_{12}O_{19}$ nanoparticles synthesized by co-precipitation method. However, the crystallite size of pure MgO is 21.6 nm and ranges between 18.9 and 25.9 nm for $0.1 < x \leq 1$. Similar results were reported by Kandregula et al. [29] (18 nm) and Ali et al. [12] (20.75 nm) for pure MgO nanoparticles synthesized by co-precipitation method. The average crystallite size for the four nanocomposites was also tabulated and the maximum value was reported for $x = 0.4$ (24.43 nm).

The morphological and the microstructural analysis of $(BaFe_{12}O_{19})_{1-x}/(MgO)_x$ nanocomposites, for $x = 0$, 0.1, 0.2, 0.4, 0.8 and 1, were investigated through transmission electron microscope (TEM). TEM micrographs for

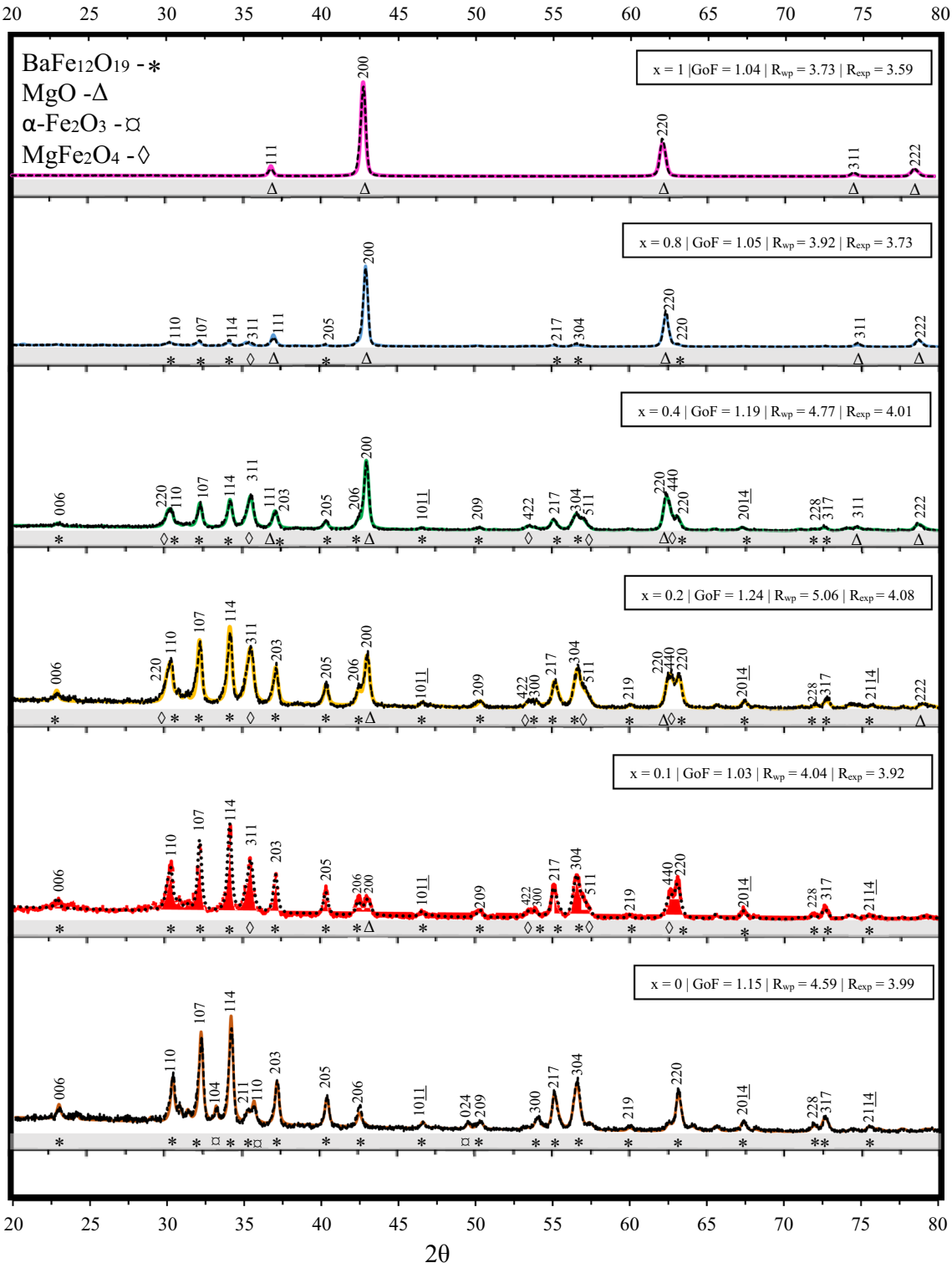

Fig. 1 XRD patterns of $(BaFe_{12}O_{19})_{1-x}/(MgO)_x$ ($x=0$, 0.1, 0.2, 0.4, 0.8 and 1) nanocomposites, where the dotted line represents the original data ands the solid line represents the refined data

all samples are shown in Fig. 4. In Fig. 4a, the micrograph of barium hexaferrite ($x=0$) shows the co-existence of spherical and nanorod shaped particles. Similar morphology was observed by Yensano et al. [17]. They reported the morphology change from spherical to rod-like of $BaFe_{12}O_{19}$ nanoparticles for a calcination temperature

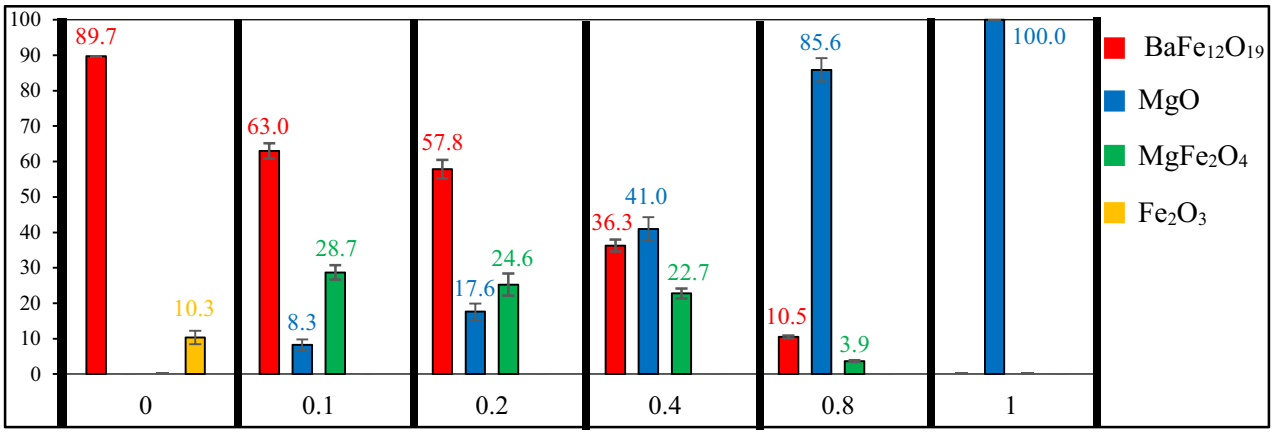

Fig. 2 Histogram showing the weight percentages of $(BaFe_{12}O_{19})_{1-x}/(MgO)_x$ ($x=0$, 0.1, 0.2, 0.4, 0.8 and 1) nanocomposites using MAUD software

Table 1 The atomic percentages of Ba, Mg, Fe and O calculated theoretically (*T*), from MAUD (*M*) and from EDX (*E*)

x	0			0.1		0.2		0.4			0.8		1		
	T	*M*	*E*	*T*	*M*	*T*	*M*	*T*	*M*	*E*	*T*	*M*	*T*	*M*	*E*
Ba	3.1	2.8	3.5	2.6	1.8	2.2	1.4	1.5	0.8	0.9	0.4	0.2	0.0	0.0	0.0
Mg	0.0	0.0	0.0	8.0	10.8	15.1	17.3	26.7	29.2	33.7	43.7	45.8	50.0	50.0	46.0
Fe	37.5	37.8	37.9	31.5	30.0	26.2	25.1	17.5	16.0	13.6	4.8	3.2	0.0	0.0	0.0
O	59.4	59.4	58.5	57.9	57.5	56.6	56.3	54.4	54.0	51.8	51.2	50.8	50.0	50.0	54.0

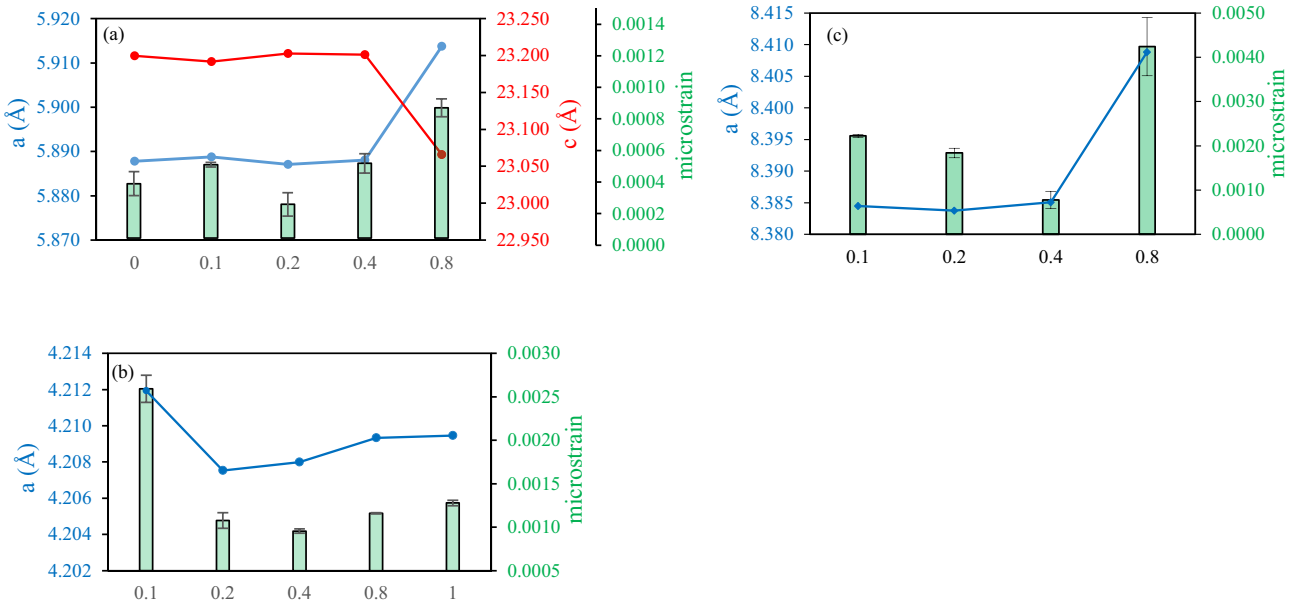

Fig. 3 The change in the lattice parameters and microstrain as a function of *x* for **a** $BaFe_{12}O_{19}$, **b** MgO and **c** $MgFe_2O_4$ phases

Table 2 The crystallite size of $BaFe_{12}O_{19}$, $MgFe_2O_4$, and MgO $(BaFe_{12}O_{19})_{1-x}/(MgO)_x$ ($x = 0$, 0.1, 0.2, 0.4, 0.8 and 1)

x	Phases	Crystallite size D (nm)	Average crystallite size (nm)
0	$BaFe_{12}O_{19}$	25.46	25.46
	α-Fe_2O_3		
0.1	$BaFe_{12}O_{19}$	21.90	20.41
	$MgFe_2O_4$	21.18	
	MgO	18.92	
0.2	$BaFe_{12}O_{19}$	21.85	20.73
	$MgFe_2O_4$	21.44	
	MgO	19.60	
0.4	$BaFe_{12}O_{19}$	23.57	24.43
	$MgFe_2O_4$	23.08	
	MgO	25.90	
0.8	$BaFe_{12}O_{19}$	24.45	24.28
	$MgFe_2O_4$	18.97	
	MgO	24.12	
1	MgO	21.55	21.55

$T > 900$ °C. Also, Wang et al. [30] stated the rod-like morphology of $BaFe_{12}O_{19}$ nanoparticles annealed at 800 °C, and this was attributed to the particular crystallographic surfaces of $BaFe_{12}O_{19}$ nanocrystals during the controlled growth processes.

For small MgO content, $x = 0.1$, 0.2 and 0.4, the particles showed a spherical shape. However, cubic morphology was detected for higher MgO content ($x = 0.8$) and for pure MgO [31]. By using ImageJ, the average particle size of the samples was estimated via the size distribution plots, shown in Fig. 5. The size of $BaFe_{12}O_{19}$ is about 90 nm [19] and that for MgO is 59 nm [32]. As for the four nanocomposites, the particle size ranged between 70 and 122 nm. The maximum particle size was abstained for $x = 0.4$. The reason might be due to the agglomeration of the two main phases with different particle sizes. The crystallite size (D_{XRD}) and the particle size (D_{TEM}) were plotted as a function of x in Fig. 6. The similar trend for both sizes might be attributed to the fact that large sized particles enhance the growth of bigger crystallite sizes.

For further morphological analysis, high resolution transmission electron microscopy (HRTEM) with the selected area of electron diffraction (SAED) were done and shown in Fig. 4. In Fig. 4c, the SAED patterns of all samples show the spotty ring pattern, which is a typical feature of polycrystalline material [33]. The d-spacing, which is the distance between successive parallel planes of atoms, is calculated from these images with the corresponding miller indices confirmed the existence of the $BaFe_{12}O_{19}$ and MgO along with $MgFe_2O_4$. The determined values are well consistent with that obtained from XRD analysis. The HRTEM images for all samples are shown in Fig. 4b. HRTEM image for pure $BaFe_{12}O_{19}$ confirmed the result of SAED where different planes with different orientations are shown.

Moreover, the different crystallites that appeared in HRTEM images confirmed that the particles synthesized are formed of many crystallites. Also, the d-spacing obtained from HRTEM images were very close to that calculated from XRD analysis and from literature [34, 35]. The most common value for d-spacing is 2.65 Å, corresponding to (111) planes that are the most preferred orientation of $BaFe_{12}O_{19}$ phase. For $x = 0.2$, the d-spacing (2.53 Å) is very close to the spacing of (311) planes, the most preferred orientation in $MgFe_2O_4$ phase [36]. This result confirms the existence of this minor phase as depicted in XRD analysis.

For $x = 0.8$ and $x = 1$, the calculated d-spacing indicated the preferred orientation of the (200) planes of MgO. This affirms the good crystallinity of the prepared samples which matches very well with XRD analysis.

The Raman spectra for pure $BaFe_{12}O_{19}$, MgO and $(BaFe_{12}O_{19})_{0.6}/(MgO)_{0.4}$ nanocomposite have been recorded between 100 and 3500 cm^{-1} at room temperature, as shown in Fig. 7a. The presence of apparent sharp peaks for pure barium hexaferrite below 700 cm^{-1} in the Raman spectra supports the crystalline nature of the prepared $BaFe_{12}O_{19}$ nanoparticles [37]. According to the group theory, 64 atoms in a unit cell of M-type Barium hexaferrite compound with space group P63/mmc may give rise to 189 optical modes including 42 Raman active modes ($11A_{1g} + 14E_{1g} + 17E_{2g}$) at room temperature [38]. The deconvoluted Raman spectrum of $BaFe_{12}O_{19}$ is shown in Fig. 7b. The bands at 717 cm^{-1} and 681 cm^{-1} are related to A_{1g} vibration at the $4f_1$ and 2b sites, respectively. The band at 613 cm^{-1} reflects the A_{1g} vibration at the $4f_2$ site; However, the band at 413 cm^{-1} is due to A_{1g} vibration at the 12 k and 2a sites. The bands at 179 cm^{-1} and 167 cm^{-1} are attributed to E_{1g} vibration of whole spinel blocks. The remaining bands at 523, 466, 385, 344, 312, and 284 cm^{-1} are attributed to the vibration of Fe–O bonds of all the octahedra at the 12 k,2a, and $4f_2$ sites [39, 40]. Moreover, the peak at 211 cm^{-1} might be due to $3F_{2g}$ mode of α-Fe_2O_3 as reported by Mallesh et al. [41].

The Raman spectrum, for pure MgO, showed a peak with high intensity around 1360 cm^{-1} and a signature of a peak with much lower intensity at 1900 cm^{-1}. This result is comparable to that reported by Weible et al. [42]. Athar et al. [43] also reported that the peak below 1500 cm^{-1} is associated to D-band, whereas the peak above 1500 cm^{-1} is for G-band of MgO nanoparticles.

For the nanocomposite sample, almost the same peaks are observed for $BaFe_{12}O_{19}$ phase with a small shift towards higher wavenumbers. The reason behind this could be attributed to the change in the microstrain accompanied by a change in lattice parameters as reported in literature[43, 44]. The peak associated to MgO at 1360 cm^{-1} still barely

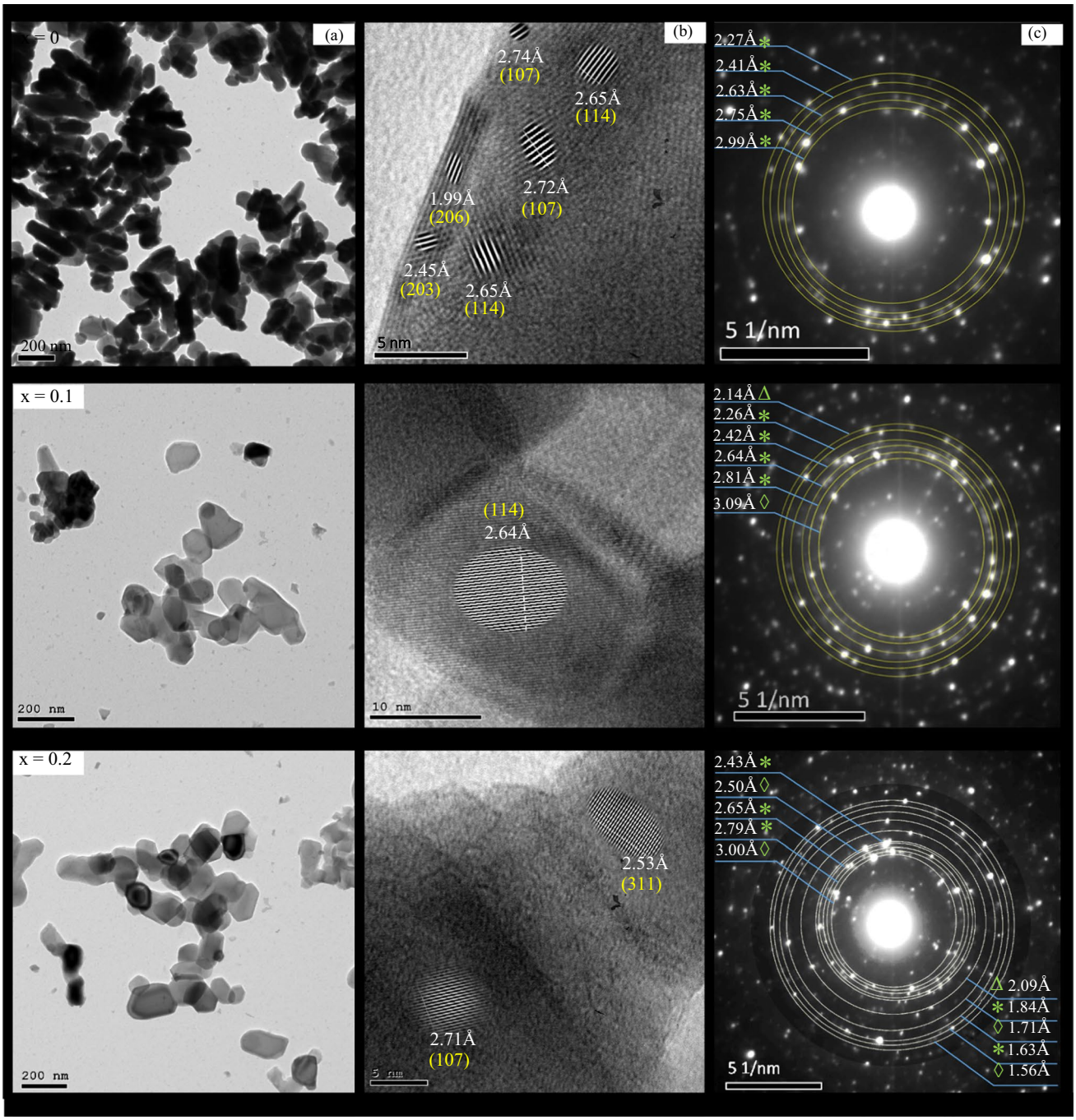

Fig. 4 **a** Transmission electron micrographs (TEM), **b** high resolution transmission electron microscopy (HRTEM) and **c** selected area of electron diffraction (SAED) of $(BaFe_{12}O_{19})_{1-x}/(MgO)_x$ ($x = 0$, 0.1, 0.2, 0.4, 0.8 and 1) nanocomposites calcinated at 950 °C. The symbols assigned for $BaFe_{12}O_{19}$, $MgFe_2O_4$ and MgO phases are asterisk, empty diamond and empty triangle, respectively

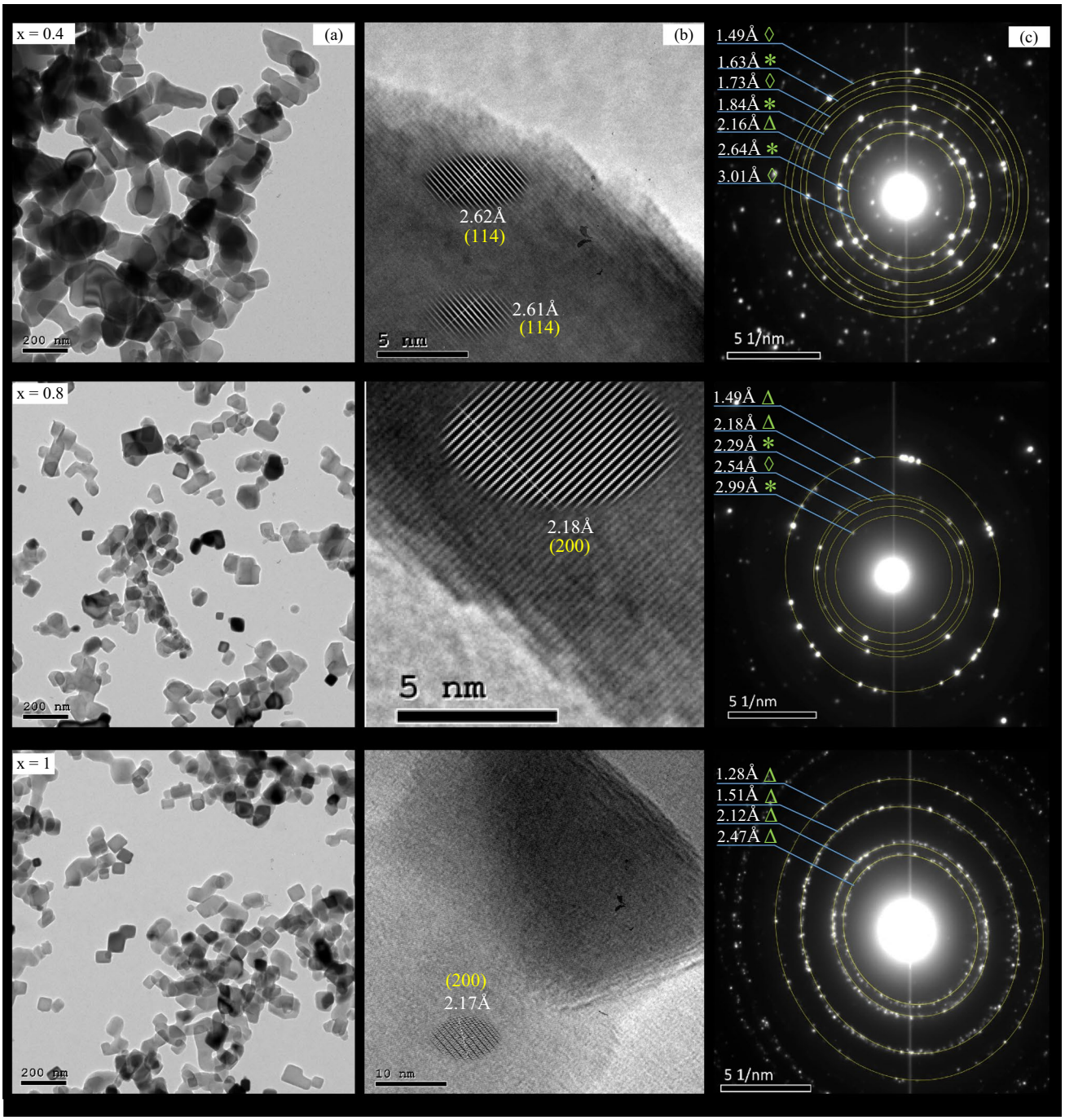

Fig. 4 (continued)

exists due to the lower weight percentage, whereas the peak at 1900 cm^{-1} disappears. Additional peaks are observed at 484 cm^{-1} and 548 cm^{-1} and are related to asymmetric stretching of metal and oxygen and asymmetric bending of oxygen in $MgFe_2O_4$, respectively [45, 46]. This confirms the existence of the minor phase as revealed in XRD analysis.

SEM image for pure $BaFe_{12}O_{19}$ shows amorphous surface and the particles are welded together and have no clear shape and boundaries. However, pure MgO nanoparticles have a smooth surface, regular morphology and clear boundaries with more voids [47]. Obviously, MgO particles seemed to be smaller than $BaFe_{12}O_{19}$, consistent with TEM micrographs. For $(BaFe_{12}O_{19})_{0.6}/(MgO)_{0.4}$ nanocomposite, the addition of MgO altered the morphology of pure ferrite as the surface of the grains became smooth with clear boundaries and larger voids. In addition,

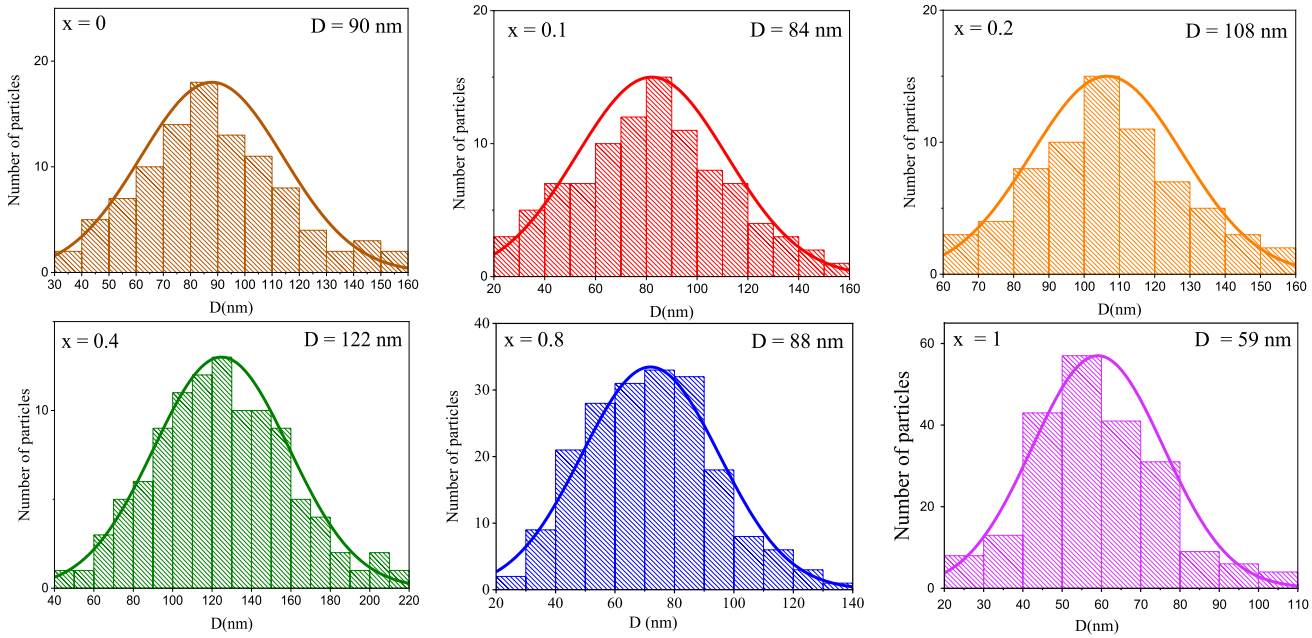

Fig. 5 Size distribution histograms for $(BaFe_{12}O_{19})_{1-x}/(MgO)_x$ ($x=0$, 0.1, 0.2, 0.4, 0.8 and 1) nanocomposites

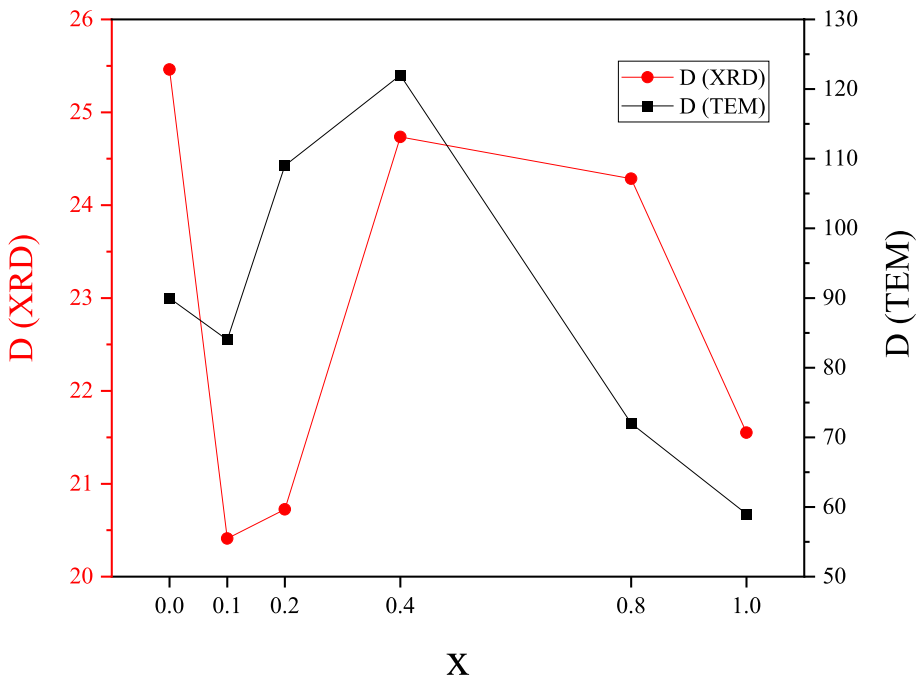

Fig. 6 D_{XRD} and D_{TEM} as a function of MgO content

the size of the particles for the nanocomposite sample was larger than both pure samples, which agrees with TEM analysis.

The elemental compositions of $(BaFe_{12}O_{19})_{1-x}/(MgO)_x$ nanocomposites, for $x=0$, 0.4 and 1, were determined using the energy dispersive X-ray spectroscopy (EDX). For pure $BaFe_{12}O_{19}$, shown in Fig. 8a, sharp peaks related to barium, iron and oxygen are obtained with no detected impurity elements. Similar results were obtained by Brightlin et al. [48] upon studying the effect of annealing temperature on the synthesis of barium hexaferrite nanoparticles. However, EDX spectrum for pure MgO revealed two sharp peaks for Mg and O as shown in Fig. 8b. This is consistent to the results reported by Mirza et al. [49] that synthesized MgO nanoparticles by co-precipitation technique. For $(BaFe_{12}O_{19})_{0.6}/(MgO)_{0.4}$ nanocomposite, the absence of

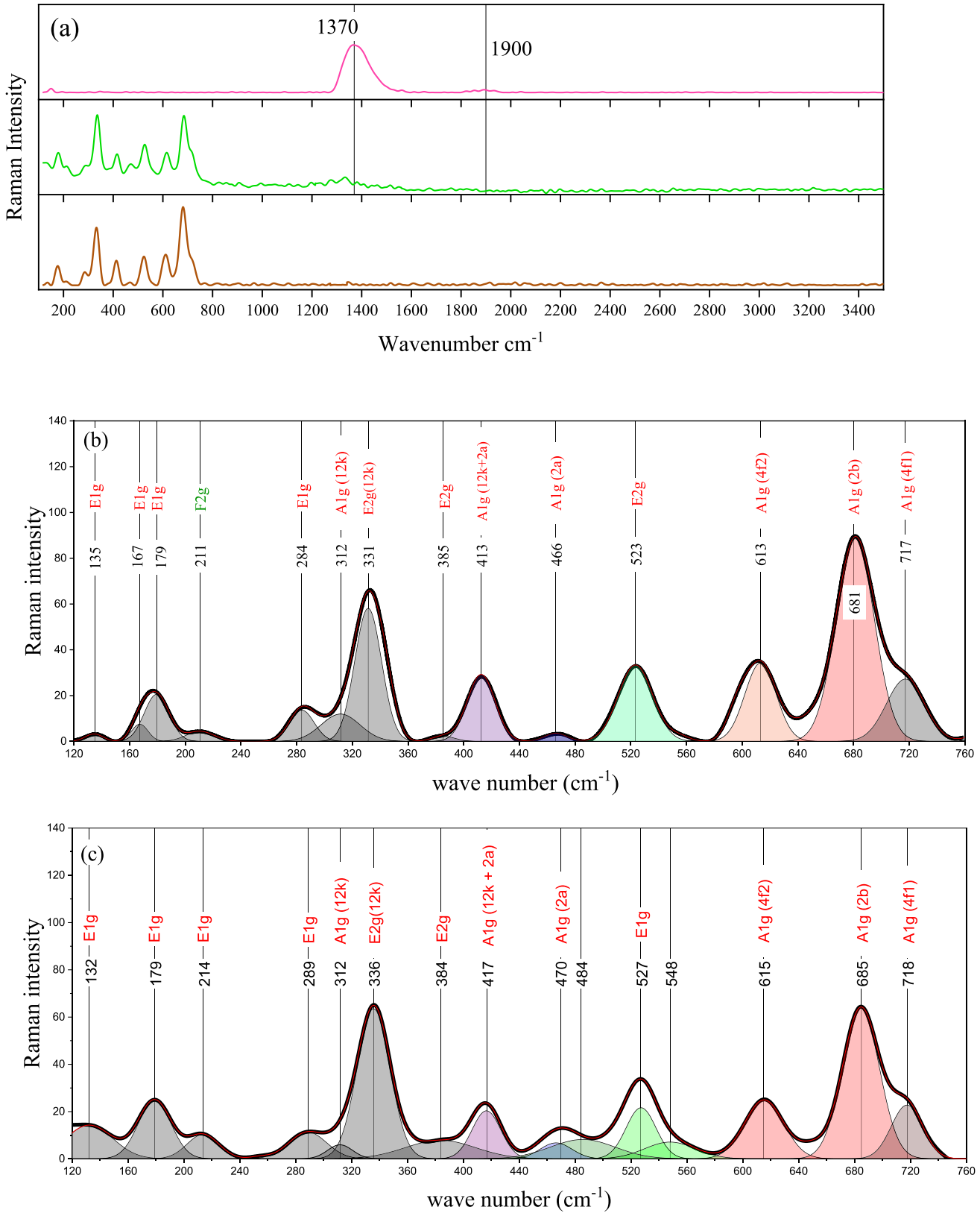

Fig. 7 The Raman spectra for **a** full Raman spectra for pure barium hexaferrite ($x=0$), pure MgO ($x=1$) and the nanocomposite ($x=0.4$), **b** deconvoluted spectrum for $x=0$ and **c** the deconvoluted spectrum $(BaFe_{12}O_{19})_{0.6}/(MgO)_{0.4}$

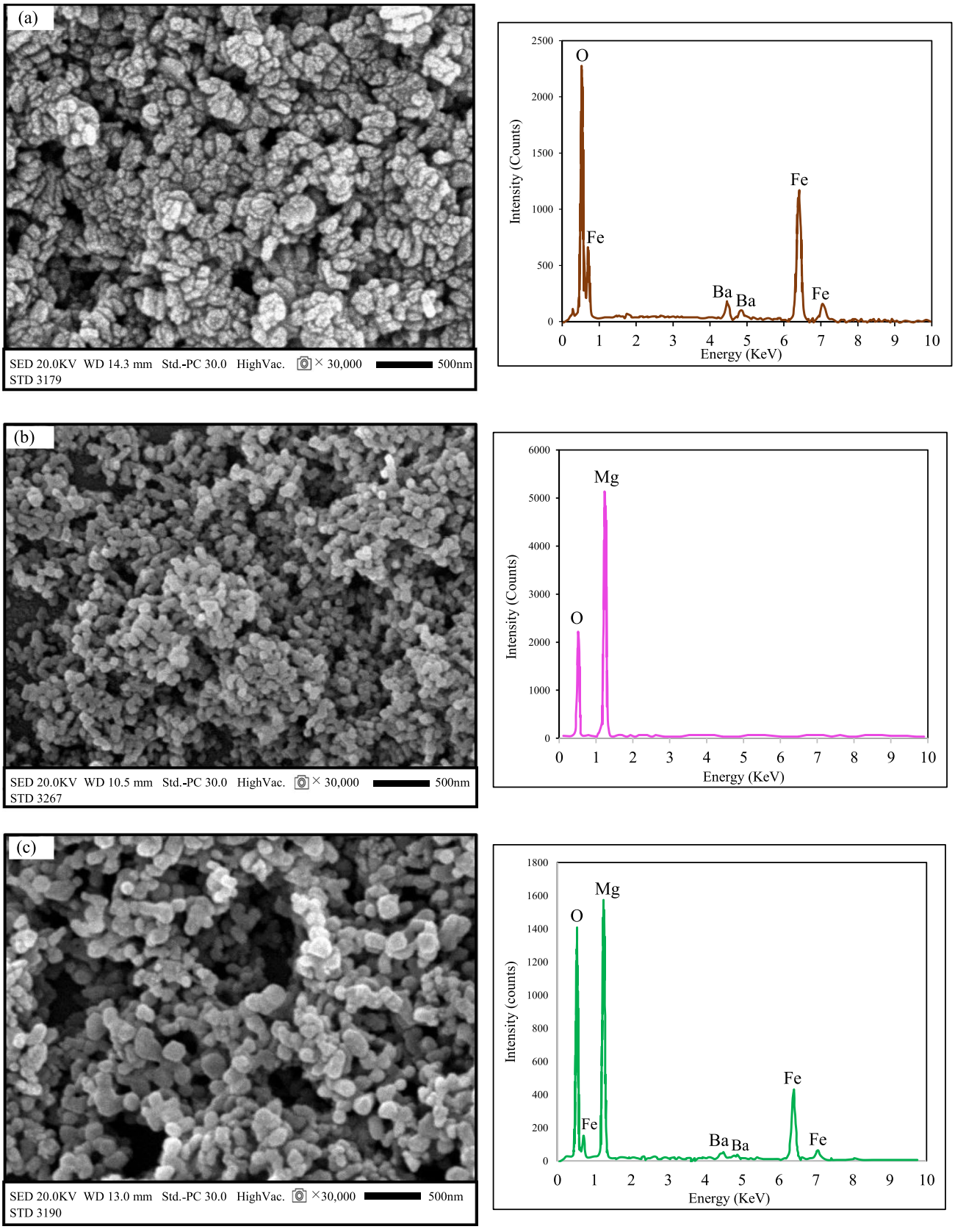

Fig. 8 SEM images and EDX spectra for pure **a** $BaFe_{12}O_{19}$ ($x=0$), **b** Pure MgO ($x=1$), and **c** 0.6Ba/0.4 Mg

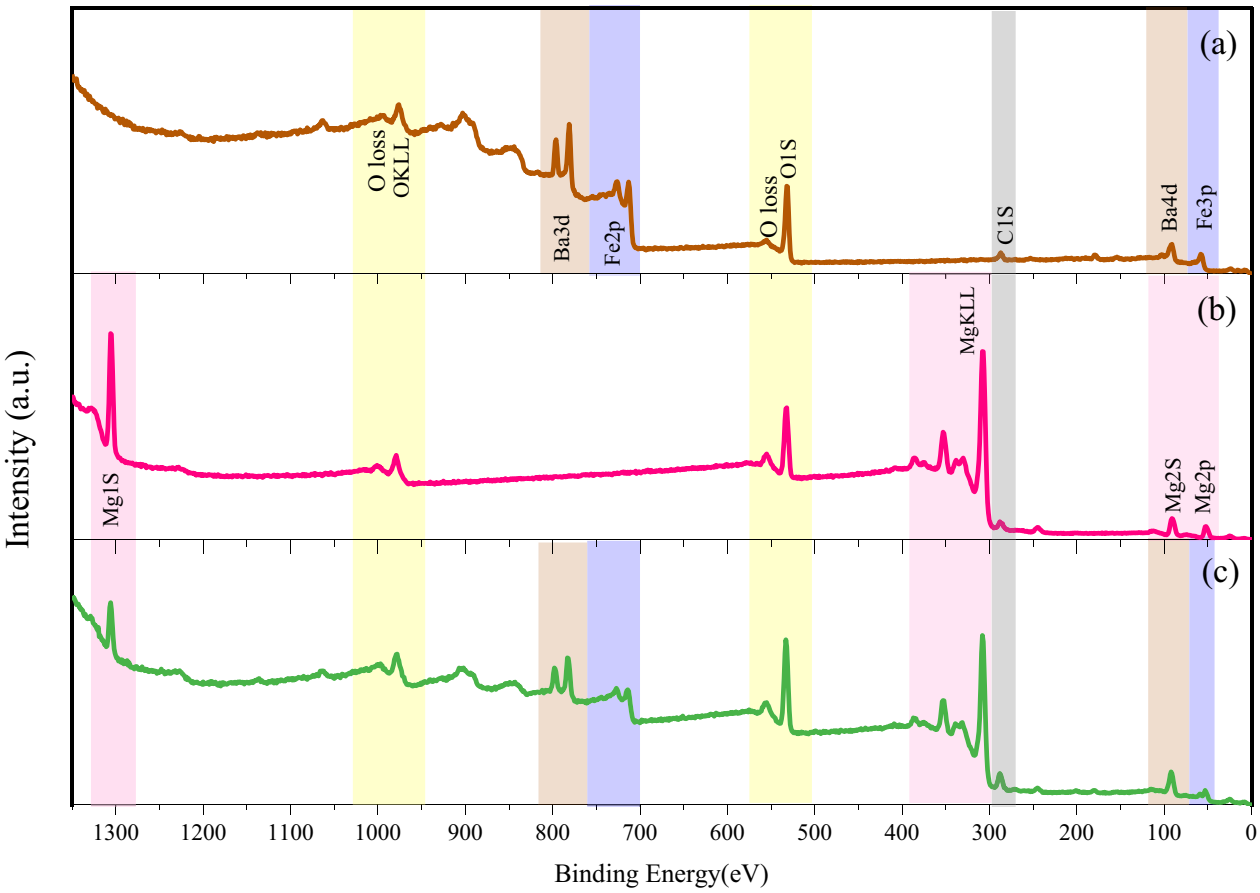

Fig. 9 High resolution XPS survey spectra of **a** pure barium hexaferrite, **b** pure MgO and the **c** $(BaFe_{12}O_{19})_{0.6}/(MgO)_{0.4}$ nanocomposite

EDX peaks related to extra elements confirms the purity and high crystallinity of the sample. This is in good agreement with XRD results where no additional phases were obtained. The elemental composition of all samples determined from EDX are listed in Table 1. The results showed a very good agreement with those calculated theoretically as well as from XRD analysis.

For the oxidation states and the elemental compositions investigation, XPS full scan spectra were performed for $BaFe_{12}O_{19}$, MgO and their $(BaFe_{12}O_{19})_{0.6}/(MgO)_{0.4}$ nanocomposite. The survey spectra of the considered samples are shown in Fig. 9. The existence of Ba, Fe and O in pure $BaFe_{12}O_{19}$ was confirmed in Fig. 9a. However, Fig. 9b revealed the elements Mg, O and C in MgO. As for $(BaFe_{12}O_{19})_{0.6}/(MgO)_{0.4}$, Fig. 9c displays binding energies assigned to Ba, Fe, Mg, O and C elements. Accordingly, the absence of any additional spectral lines in the nanocomposite validates its purity. This confirms the EDX results regarding the elemental composition of the composite and affirms its formation in one matrix as revealed in XRD. The peak of C1s, O1s and OKLL were observed in the three spectra at 287 eV, 532–533 eV and 976–979 eV, respectively [49, 50]. High-resolution HR-XPS are deconvoluted to determine their oxidation states. The high-resolution XPS spectra of barium (Ba-3d) in both $BaFe_{12}O_{19}$ and the nanocomposite ($x = 0.4$), shown in Fig. 10a, demonstrated two main peaks centered at 780.1 eV and 795.4 eV, attributed to Ba-3d5/2 and Ba-3d3/2, respectively. In the nanocomposite sample, each of the peaks of Ba3d is deconvoluted into two other peaks named Ba1 and Ba2, as shown in Fig. 10. The binding energies for Ba3d5/2 are Ba1 = 780.0 eV and Ba2 = 782.3 eV, whereas for Ba3d3/2, Ba1 = 796.2 eV and Ba2 = 798.0 eV. The splitting between Ba1 and Ba2 is around 1.7 eV as reported by many researchers [49, 50]. Alema et al. [51], who studied the dielectric properties of $BaMg_{1/3}Nb_{2/3}O_3$ doped $Ba_{0.45}Sr_{0.55}TiO_3$, reported that the peak Ba1 obtained in XPS analysis is associated to Ba atoms in perovskite, whereas Ba2 peak is related to Ba atoms in BST nonperovskite environment, such as carbonates, oxides, and relaxed BST phases due to oxygen vacancy and residual defects.

In our study, the change of position of the Ba atoms is possible because of the carboxylic groups formed on the

surface contain oxygen atoms that are forming new bonds with the Ba atoms located on the surface of the nanoparticles. This modifies the chemical environment of Ba atoms (since they are forming Ba–O bond not only with the O^{2-} lattice ions), which in turn, changes the charge balance in the crystalline lattice and the Ba atoms are moved to a different position (Ba2 sites) [52]. The XPS results showed that the Ba ions in the two samples ($x=0$ and $x=0.4$) are in the Ba^{2+} state [17].

Figure 10b shows the Fe-2p spectra in pure barium hexaferrite. It reveals the two main peaks belonging to Fe-2p3/2 and Fe-2p1/2. The two main peaks were then deconvoluted into two peaks giving the resultant Fe^{2+}-2p3/2(Oh), Fe^{3+}-2p3/2(Th), Fe^{2+}-2p1/2(Oh) and Fe^{3+}-2p1/2(Th). The corresponding binding energies of the obtained peaks are 711.2 eV, 713.8 eV, 724.5 eV and 727.3 eV, respectively, where Oh and Th represent the octahedral and tetrahedral sites, respectively. Zhang et al. [53] reported that high sintering temperature could induce the formation of bivalent Fe^{2+} ions from trivalent Fe^{3+}. Accordingly, at high sintering temperature, the formation of oxygen vacancies increases and thus leads to reduce the oxidation state of iron ions from Fe^{3+} to Fe^{2+} [54, 55]. Also, this result is very similar to the one obtained by Yensano et al. [17] for $BaFe_{12}O_{19}$ prepared by co-precipitation method and calcinated at 900 and 1000 °C.

O1s peaks of oxygen ions in all the samples are shown in Fig. 10c. These peaks are related to the lattice oxygen (O_L), oxygen vacancies (O_V) and oxygen hydroxyl (O_H) [56]. Mg1s peak, centered at 1306 eV for $x=0$ and $x=0.1$, is shown in Fig. 10d. In pure MgO, the deconvolution of the main peak led to two peaks at 1303.1 eV and 1305.3 eV. However, in the nanocomposite, the Mg1s peak is deconvoluted into three peaks at 1303.2 eV, 1304.8 eV and 1306.3 eV. It was clear that there is a peak in common (~ 1303 eV) which might be attributed to a small percentage of $Mg(OH)_2$ formed on the surface of the nanoparticles as reported by Zambrano et al. [57]. The splitting of the second peak at 1305.3 eV is attributed to the formation of $MgFe_2O_4$ as a secondary phase (1304.8 eV) and the main phase MgO (1306.3 eV). As listed in Table 3, it is clear that the binding energies for Mg1s in the nanocomposite sample were very close to the values obtained by Lu et al. [58] who reported that the binding energy of MgO is observed to be 1306.6 eV and reduced to 1303.8 eV in $MgFe_2O_4$.

The magnetic behavior of pure $BaFe_{12}O_{19}$ and MgO nanoparticles and their nanocomposites is investigated at room temperature via M-H hysteresis loops, with a magnetic field H varying between − 20,000 G and 20,000 G. The magnetization as a function of the applied field of pure $BaFe_{12}O_{19}$ and MgO are shown in Fig. 11. As reported by many researchers, $BaFe_{12}O_{19}$ nanoparticles has a high curie temperature about 723 K, after which, its ferromagnetic properties start to change. Specifically, the material undergoes a phase transition from a ferromagnetic state to a paramagnetic state [57–59]. As per our study the pure barium hexaferrite nanoparticles annealed at 950 °C, revealed hard ferromagnetic behavior at room temperature [60, 61]. This behavior decreases with the increase in the concentration of MgO, which showed a very weak ferromagnetic behavior with a diamagnetic behavior at high fields. However, *M–H* loops for $BaFe_{12}O_{19}$ and the four nanocomposites show a kink behavior. This behavior is typically associated to the presence of hard and soft magnetic phases in the nanocomposite. It arises due to the different magnetic responses of the hard and soft phases to an applied magnetic field [23]. The hard magnetic phase typically exhibits a higher coercivity, representing its resistance to magnetization reversal, while the soft magnetic phase has a lower coercivity and is more easily magnetized. During magnetization, when the external magnetic field is gradually increased, the soft phase starts to align with the field, leading to an increase in the magnetization. However, as the external field continues to increase, the hard phase starts to align as well, contributing to an additional increase in the overall magnetization of the nanocomposite. At a certain critical field, the magnetization curve experiences a sudden change or kink as reported by Attyabi et al. [62]. This is usually followed by a steep increase in the magnetization until the saturation point is reached. A study was done by Manglam et al. [63] on the magnetic properties of barium hexaferrite (hard) and cobalt zinc ferrite (soft) nanocomposites, and a kink behavior has been noticed in all the nanocomposites. They attributed this behavior to the individually switching of the soft magnetic phase at a lower magnetic field than that of the hard magnetic phase. Algarou et al. [64] also studied the magnetic properties of hard/soft nanocomposites and observed the same kink behavior in the *M–H* loops. They related this result to a separable swapping of soft and hard magnetic phases because of incomplete exchange-coupling among them and thus, a superimposition of two loops will be noticed. As per our study, the observed kink behavior of the *M–H* loops is due to the existence of $BaFe_{12}O_{19}/Fe_2O_3$ ($x=0$) and $BaFe_{12}O_{19}/MgFe_2O_4$ in the nanocomposites ($x=0$, 0.1, 0.2, 0.4 and 0.8) as reported in XRD analysis.

Three different kinds of magnetic behavior (soft/soft, hard/hard, and soft/hard) related to grain interfaces and magnetic interactions exist in hexagonal/spinel ferrite systems. The major interaction is the exchange–coupling interaction between soft/hard phases, while the other interactions are dipolar between the hard/hard phases in hexagonal ferrite and soft/soft phases in the spinel system [65]. The dM/dH of demagnetization curve, which provides a suitable criterion for exchange coupling, is displayed in Fig. 12. It is clearly seen that for all samples, except for pure MgO, two

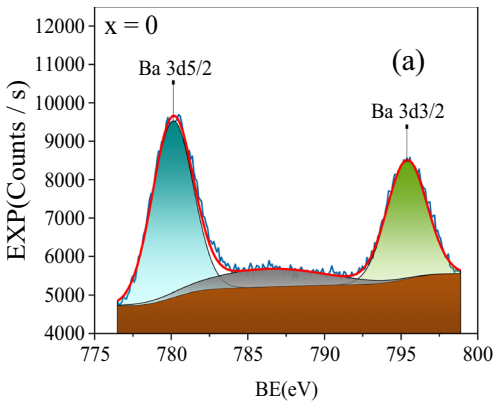
x = 0
(a)
Ba 3d5/2
Ba 3d3/2
EXP(Counts / s)
BE(eV)

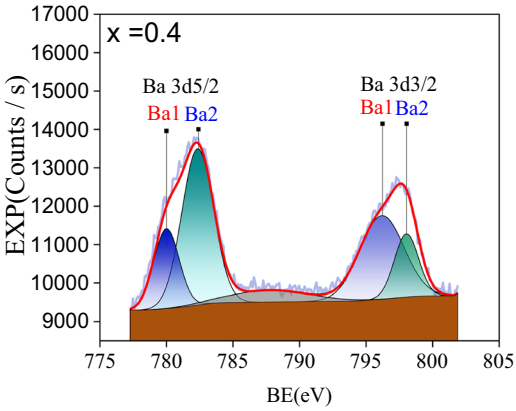
x =0.4
Ba 3d5/2
Ba1 Ba2
Ba 3d3/2
Ba1 Ba2
EXP(Counts / s)
BE(eV)

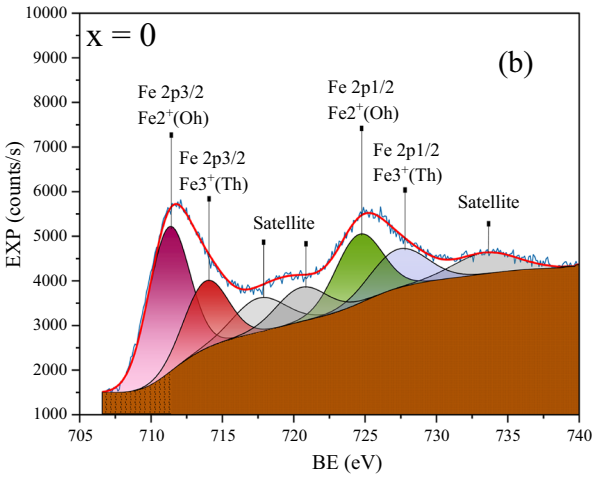
x = 0
(b)
Fe 2p3/2
Fe2+(Oh)
Fe 2p3/2
Fe3+(Th)
Satellite
Fe 2p1/2
Fe2+(Oh)
Fe 2p1/2
Fe3+(Th)
Satellite
EXP (counts/s)
BE (eV)

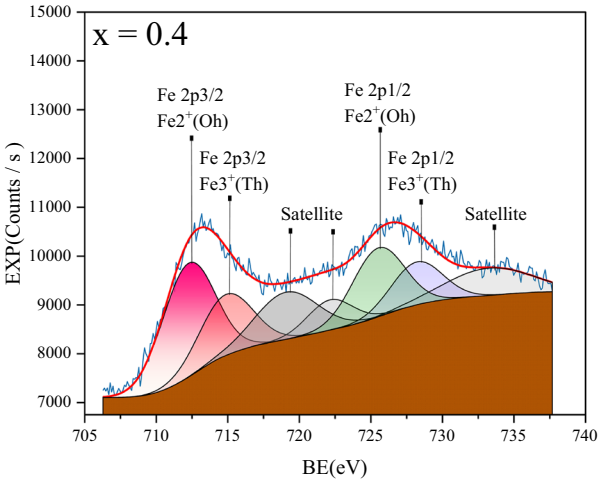
x = 0.4
Fe 2p3/2
Fe2+(Oh)
Fe 2p3/2
Fe3+(Th)
Satellite
Fe 2p1/2
Fe2+(Oh)
Fe 2p1/2
Fe3+(Th)
Satellite
EXP(Counts / s)
BE(eV)

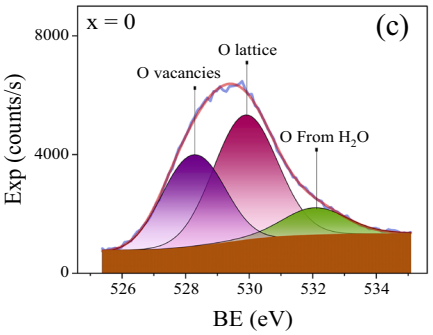
x = 0
(c)
O lattice
O vacancies
O From H2O
Exp (counts/s)
BE (eV)

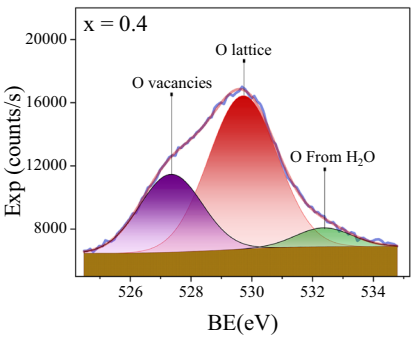
x = 0.4
O lattice
O vacancies
O From H2O
Exp (counts/s)
BE(eV)

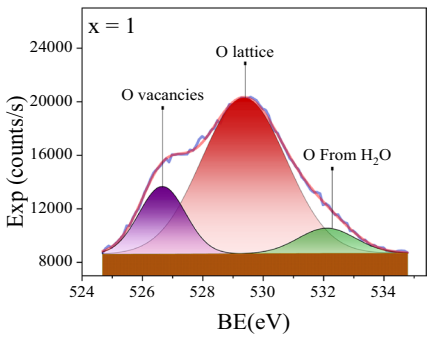
x = 1
O lattice
O vacancies
O From H2O
Exp (counts/s)
BE(eV)

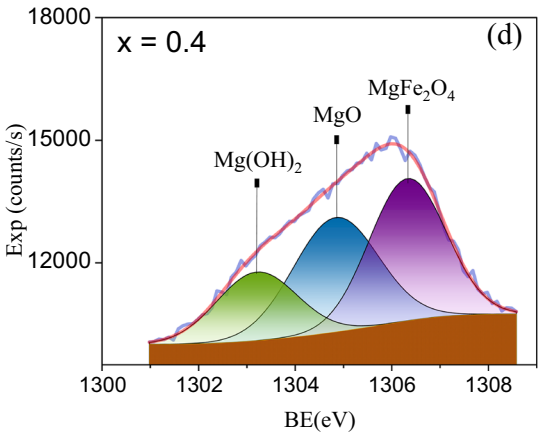
x = 0.4
(d)
MgFe2O4
MgO
Mg(OH)2
Exp (counts/s)
BE(eV)

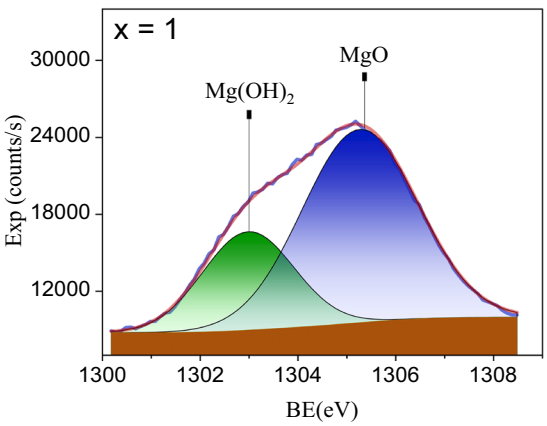
x = 1
MgO
Mg(OH)2
Exp (counts/s)
BE(eV)

◂**Fig. 10** The deconvolution of the main spectra lines of **a** Ba-3d, **b** Fe-2p, **c** O-1s and **d** Mg-1s

peaks were observed. For pure $BaFe_{12}O_{19}$, the two peaks are located at 800 G and 6200 G. Whereas, for the nanocomposites, the peaks are located at 300 G and 5750 G. These peaks verify that the hard $BaFe_{12}O_{19}$/soft Fe_2O_3 (for $x=0$) and hard $BaFe_{12}O_{19}$/soft $MgFe_2O_4$ (for $x=0.1$, 0.2, 0.4 and 0.8) are not well couple-exchanged [66], and this led to the kink behavior of the *M–H* loops. For further analysis, the ΔH versus M curves for $x=0$, 0.1, 0.2, 0.4 and 0.8 are also plotted and shown in Fig. 13. All the samples did not show a squeezing effect as all the curves are bell shape. The maximum width was obtained at magnetization zero. This is similar to the result obtained by Mangam et al. [67] who studied the magnetic interaction between BHF/CZF nanocomposites, and found that the squeezing effect was present at room temperature and vanishes at temperatures below 200 K due to insufficient magnetic biasing between the hard and soft phases. Similarly, a study was done by Datta et al. [68] on the nanocomposites of hard magnetic barium hexaferrite and soft magnetic Ni–Mn–S. A squeezing effect was observed at room temperature for ball milling time 2 h, 4 h and 8 h, and vanishes below 2 h.

In order to find the saturation magnetization of pure MgO, the ferromagnetic magnetization (M_f) was first obtained using Eq. (2) [69]:

$$M_f = M - \boldsymbol{\chi_p} H, \tag{2}$$

where $\boldsymbol{\chi_p}$ is the slope at high H (the high field susceptibility). The result is shown in the inset of Fig. 11.

At high magnetic field and below Curie temperature, the magnetization may be expressed using Eq. (3) [70]:

$$M = M_s\left(1 - \frac{\beta}{H^2}\right). \tag{3}$$

The magnetization M was plotted versus $1/H^2$ for all the samples, shown in Fig. 14, from which M_s was estimated by extrapolating the plot to $1/H^2=0$. The figures showed a linear fit from which the parameters M_s, M_r, H_c, and squareness (SQR) for all the samples are extracted and recorded in Table 4.

The pure barium hexaferrite sample have a saturation magnetization $M_s=43.7$ emu/g, $M_r=19.2$ emu/g and coercivity $H_c=4595.5$ G [71]. Similar behaviour was reported by Mosleh et al. [72] when studying the effect of annealing temperature on the magnetic properties of $BaFe_{12}O_{19}$ nanoparticles. They reported the slight decrease of M_s as the annealing temperature increased above 900 °C. The kink that appeared in the hysteresis loop may be attributed to the wide distribution of particle size between 20 and 160 nm as revealed in TEM [73]. Another study was conducted by Wang et al. [30] on $BaFe_{12}O_{19}$ nanoparticles synthesized by hydrothermal method and calcinated at 800 °C. The obtained values for M_s and H_c were 67.3 emu/g and 4511 Oe, respectively. The factors resulting in high H_c value was related to the shape anisotropy of the $BaFe_{12}O_{19}$ nanorods due to the deviation from sphericity [74]. This was observed in pure barium ferrite and confirmed by TEM. For pure MgO, $M_s=0.06$ emu/g, $M_r=0.011$ emu/g and $H_c \approx 150$ G. These results are similar to that obtained by Phokha et al. [75] for MgO nanoparticles of 25 nm size. Also, Azzaza et al. [76] reported a comparable value of M_s (0.0026 emu/g) for a size of 11.9 nm. This weak ferromagnetism was also reported by Parveen et al. [77]. The magnetism in MgO nanoparticles has been mainly attributed to the defect induced effects in the sample [78]. Kumar et al. [79] reported the ferromagnetism of MgO nanoparticles because of Mg vacancies. Moreover, Gao et al. [80] studied the defect induced magnetism in MgO nanoparticles and suggested that the induced magnetic moment was due to the spin-polarization of 2p electrons of O atoms near Mg vacancies and not due to oxygen vacancies. Accordingly, the ferromagnetism in MgO nanoparticles might be due to the Mg vacancies confirmed by EDX results for pure MgO Phase. Moreover, this vacancy can be confirmed by the formation of small percentage of $Mg(OH)_2$ as revealed by the XPS spectrum.

For the remaining four nanocomposites ($x=0.1$, 0.2, 0.4 and 0.8), it is clear from the Table 4 that the saturation and remanent magnetizations decreased with x as shown in Fig. 15. Another two plots are also drawn on the same figure that correspond to $(1-x)\ M_s\ (x=0)=M_s'$ and $(1-x)M_r\ (x=0)=M_r'$ as a function of x; where $(1-x)$ is the weight % of $BaFe_{12}O_{19}$ phase and M_s $(x=0)$ and M_r $(x=0)$ are the saturation magnetization and remanent magnetization for pure $BaFe_{12}O_{19}$ respectively. These two plots seemed to be very close to that of $M_s(x)$ and $M_r(x)$, meaning that the saturation and remanent magnetizations are almost due to only $BaFe_{12}O_{19}$ and $MgFe_2O_4$ phases, for $x=0$, 0.1, 0.2, 0.4 and 0.8, knowing that MgO had a very weak ferromagnetic behavior compared to these two phases. Hence, M_s and M_r can be controlled by the amount of MgO nanoparticles present in the sample. A similar result was reported by Ali et al. [12] who studied the magnetic hysteresis of xMgO/$(1-x)$ $CuFe_2O_4$ nanocomposites. They found that the superparamagnetic behavior of $CuFe_2O_4$ remains invariant, but M_s decreases with increase in MgO concentration. This is due to the increase in the content of nonmagnetic ion which in turns reduces the saturation magnetization. Another study was performed by Widodo et al. [81] about the magnetic properties of $BaFe_{12}O_{19}/SrTiO_3$ based composites. They found that remanent and saturation magnetization values of composite samples decreased with increasing fraction of STO components as STO is non-magnetic. Moreover, Cao et al. [82] studied the magnetic properties of $BaFe_{12}O_{19}$/

Table 3 The binding energy (BE) and the area of the de-convoluted core energy levels of Ba, Fe, O and Mg in the pure $BaFe_{12}O_{19}$, pure MgO and the nanocomposite ($x=0.4$)

Core energy levels		Assignment	Pure $BaFe_{12}O_{19}$ ($x=0$)		Pure MgO ($x=1$)		Nanocomposite ($x=0.4$)	
			BE (eV)	Area	BE (eV)	Area	BE (eV)	Area
Ba-3d	Ba-$3d_{5/2}$	Ba^{2+}	780.1	15,241	**	**	780.0	4940
							782.3	12,083
	Ba-$3d3_{/2}$	Ba^{2+}	795.4	10,025	**	**	796.2	8955
							798.0	3724
Fe-2p	Fe-$2p3_{/2}$	$Fe^{2+}(O_h)$	711.2	11,750	**	**	712.2	10,693
		$Fe^{3+}(T_h)$	713.8	5822	**	**	714.9	5834
		Satellite	717.6/720.5	3481/3381	**	**	719.1/722.1	5255/2460
	Fe-$2p1_{/2}$	$Fe^{2+}(O_h)$	724.5	6340	**	**	725.5	6378
		$Fe^{3+}(T_h)$	727.3	4324	**	**	728.2	3922
		Satellite	733.4	2625	**	**	733.3	4223
O-1s		O_v	528.3	6762	526.5	9764	527.5	12,783
		O_L	529.8	10,558	529.7	40,872	529.9	27,579
		O_H	532.1	2482	531.9	4444	532.6	2789
Mg- s		$Mg(OH)_2$	**	**	1303.1	17,985	1303.2	3510
		$MgFe_2O_4$	**	**	**	44,515	1304.8	6223
		MgO		**	1305.3		1306.3	6915

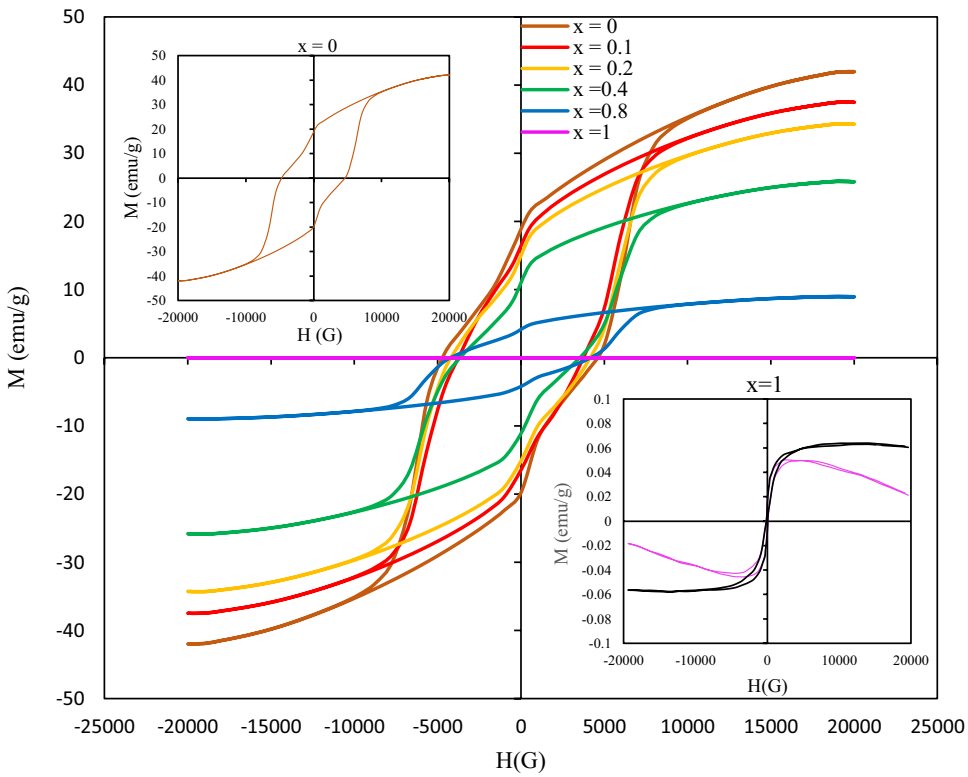

Fig. 11 *M–H* hysteresis loop of the six samples ($x=0$, 0.1, 0.2, 0.4, 0.8 and 1) at room temperature

Co_3O_4 nanocomposites calcinated at 400 °C, and reported that M_s and M_r values changed with the mass fraction of $BaFe_{12}O_{19}$ with ($M_s=56.5$ emu/g) and the two composites displayed a decreased saturation magnetization, with M_s being 37.1 emu/g and 19.4 emu/g for the samples of $BaFe_{12}O_{19}/Co_3O_4$ with mass ratios 2:1 and 1:2, respectively.

The variation of coercivity (H_c) with MgO content (x) is also plotted for all samples in Fig. 15. It is obvious that the coercivity of the four nanocomposites ranges between the pure barium hexaferrite (4595.5 G) and pure magnesium oxide (149.9 G) [6]. As reported by previous studies, the coercivity can be affected by particle size [83] as well as the

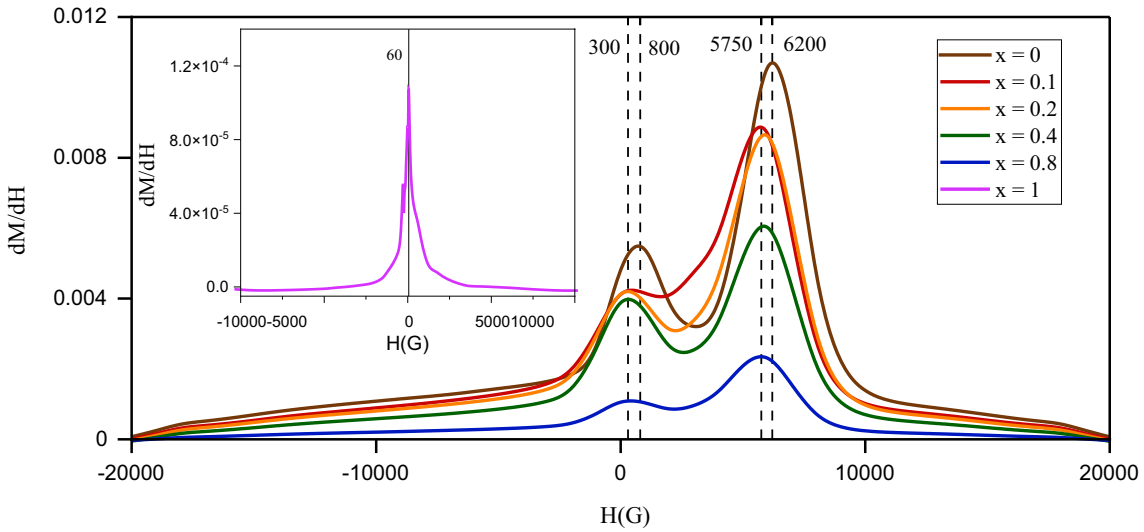

Fig. 12 d*M*/d*H* curves for all the samples at 300 K

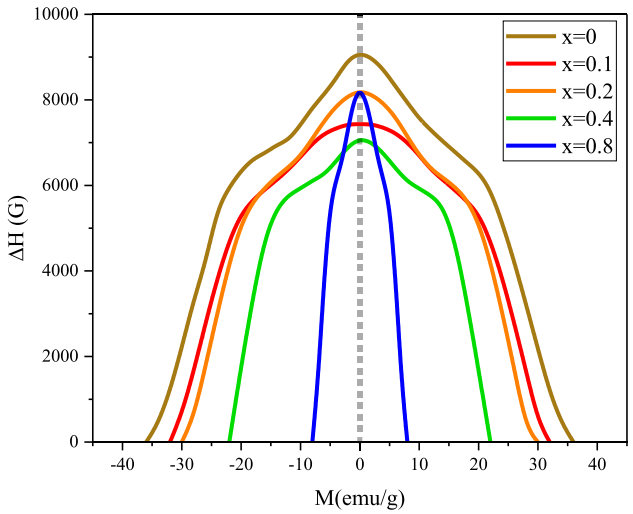

Fig. 13 Magnetization vs loop width (*M*–Δ*H*) plots at 300 K for $x=0$, 0.1, 0.2, 0.4 and 0.8

weight percentage of the different phases (hard/soft) [34]. As per our study, $BaFe_{12}O_{19}$ is hard ferromagnetic, whereas $MgFe_2O_4$ is a soft magnetic material at room temperature with curie temperature around 713 K as reported by many researchers [84, 85]. The weight percentage of $MgFe_2O_4$ with respect to $BaFe_{12}O_{19}$, denoted by *I*, is plotted in Fig. 15 and revealed an interesting behavior compared to H_c. So, it could be concluded that as *I* increases, the coercivity decreases and vice versa.

The maximum energy product $(BH)_{max}$ is a frequently used criteria for the quality of a permanent magnet [86]. To calculate $(BH)_{max}$ for the samples, the *M*–*H* loops were

Table 4 M_s, M_r and H_c area and SQR for all the samples

Sample (*x*)	M_s (emu/g)	H_c (G)	M_r (emu/g)	SQR
0	43.7	4595.5	19.2	0.439
0.1	38.8	3737.6	16.4	0.422
0.2	35.6	4137.3	15.0	0.421
0.4	26.8	3572.5	11.0	0.410
0.8	9.3	4155.4	4.2	0.451
1	0.06	149.9	0.011	0.169

transformed to *B*–*H* loops according to $B=\mu_o H+M$ [73]. Then, $(BH)_{max}$ was calculated as the area of the largest rectangle that can be inscribed under the second quadrant of the *B*–*H* loop as shown in inset(b) of Fig. 16 [87]. $(BH)_{max}$ of the pure $BaFe_{12}O_{19}$ and the four nanocomposites was calculated and are presented in Fig. 17. The maximum value of $(BH)_{max}$ was obtained for pure $BaFe_{12}O_{19}$ (27.71 kJ/m^3). As for the nanocomposites, $(BH)_{max}$ values calculated are 18.47, 11.80, 6.82 and 0.86 kJ/m^3 for $x=0.1$, 0.2, 0.4 and 0.8 respectively. As expected, $(BH)_{max}$ value decreases with the increase in the weight percentage of MgO phase.

4 Conclusion

Co-precipitation technique followed by high-speed ball milling procedure has succeeded in the synthesis of pure barium hexaferrite and pure magnesium oxide phases with their four nanocomposites. The XRD analysis showed the high crystallinity and purity for the pure samples as well

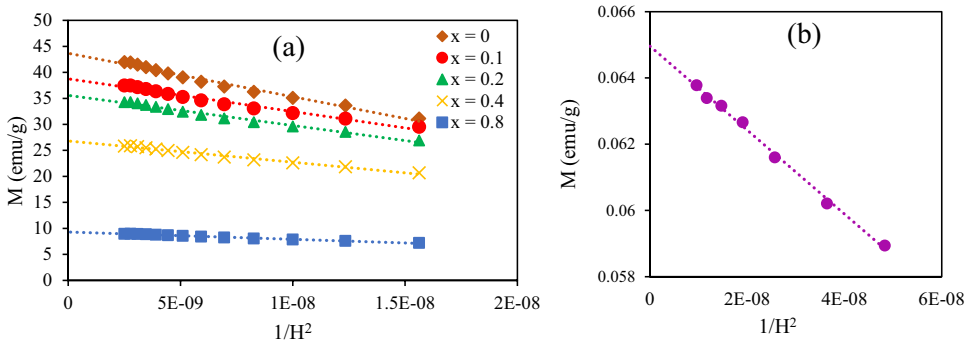

Fig. 14 M versus $1/H^2$ curve extrapolated to $1/H^2 = 0$ for **a** $x = 0$, 0.1, 0.2, 0.4 and 0.8, **b** $x = 1$

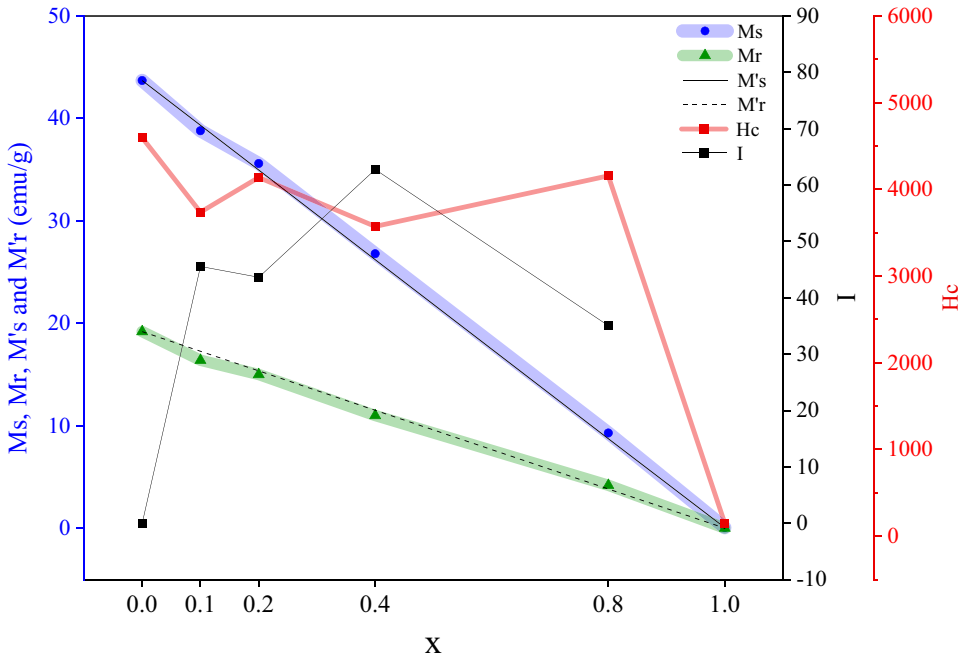

Fig. 15 M_s, M_r and H_c as a function of x

as the formation of $MgFe_2O_4$ as a minor phase in the four nanocomposites. The lattice parameters of the two phases were highly dependent on the microstrain for the composite samples. The TEM images showed the existence of rod and spherical nano particles for $BaFe_{12}O_{19}$ and changed to only spherical in the nanocomposites with the addition of MgO that showed a cubic shaped particle. The Raman spectra showed sharp peaks for $(BaFe_{12}O_{19})_{1-x}/(MgO)_x$ ($x = 0$ and 0.4) samples with blue shift of all peaks in $x = 0.4$. For $(BaFe_{12}O_{19})_{0.6}/(MgO)_{0.4}$ nanocomposite, the spectrum showed some additional peaks confirming the formation of $MgFe_2O_4$ phase. MgO Raman spectrum had a very clear high intensity peak in the pure sample, and it appeared much smaller in the nanocomposites. The elemental composition from EDX were in good agreement with the theoretical values in both pure phases and the four nanocomposites. The SEM images showed an amorphous surface for pure $BaFe_{12}O_{19}$ with small voids and the morphology became smoother after adding MgO phase in the nanocomposite $(BaFe_{12}O_{19})_{0.6}/(MgO)_{0.4}$ with larger number of voids. Moreover, in XPS, the chemical states of the elements of both pure samples and $(BaFe_{12}O_{19})_{0.6}/(MgO)_{0.4}$ nanocomposite were analyzed, demonstrating the composition elements (Ba^{2+}, Fe^{2+}, Fe^{3+} Mg^{2+} and O^{2-}), and revealed the existence of $MgFe_2O_4$ peaks in the nanocomposite sample. Finally, the magnetic study of the different samples revealed the hard ferromagnetic behavior for pure $BaFe_{12}O_{19}$ phase and the very weak ferromagnetism in pure MgO. The nanocomposites followed a clear decreasing trend in the saturation and remanent magnetization with the addition of MgO phase. However, the coercivity did not have a clear trend and attained the highest value for $(BaFe_{12}O_{19})_{0.2}/(MgO)_{0.8}$ among the four nanocomposites. The decrease in the values of $(BH)_{max}$ as the content of MgO increases verified its weak magnetic coupling with $BaFe_{12}O_{19}$.

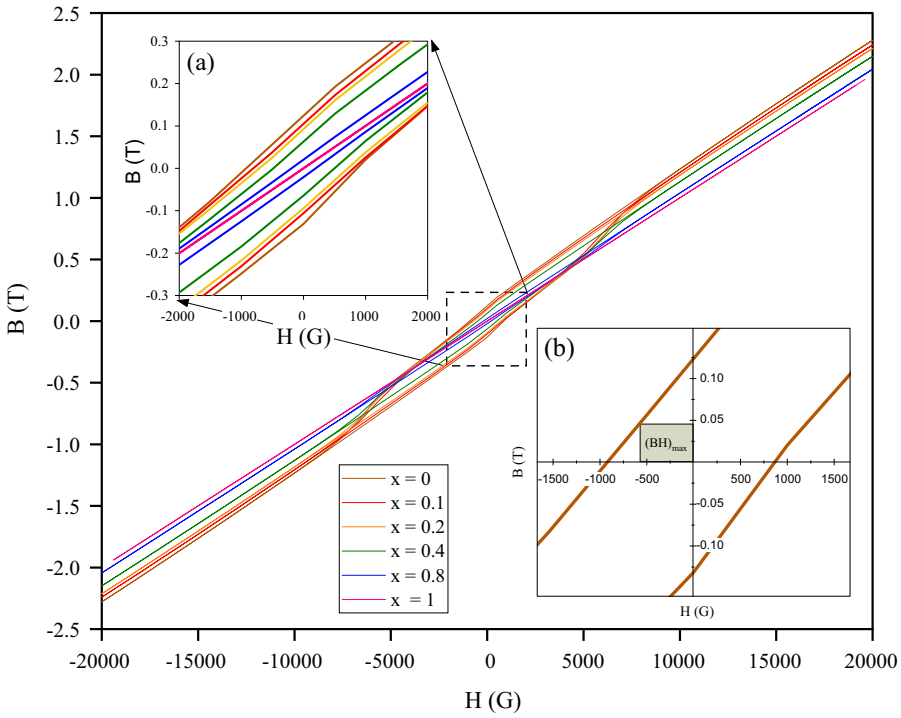

Fig. 16 Magnetic hysteresis (B–H) loops for the six samples ($x=0$, 0.1, 0.2, 0.4, 0.8 and 1) with an inset **a** showing the (B–H) loops for − 2000 G ≤ H_c ≤ 2000 G and inset **b** showing $(BH)_{max}$

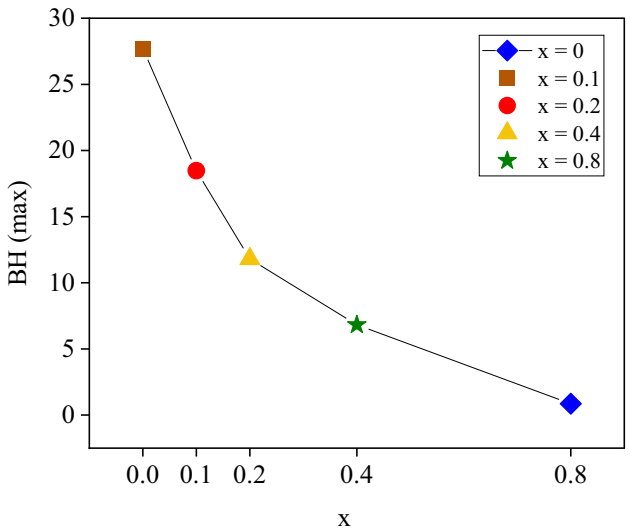

Fig. 17 $(BH)_{max}$ of pure $BaFe_{12}O_{19}$ and the four nanocomposite samples ($x=0.1$, 0.2, 0.4 and 0.8)

Acknowledgements Authors declare their genuine gratitude and appreciation to Faculty of Science at Alexandria University in Egypt, Central Metallurgical Research & Development Institute (Helwan, Egypt) and Advanced Materials Science Lab at BAU (Debbieh, Lebanon).

Author contributions MS performed the measurements, processed the experimental data, and drafted the manuscript. Prof RA and Dr. KH were involved in planning and supervised the work. Prof RA and Dr. KH discussed the results and commented on the manuscript.

Data availability The data that support the findings of this study are available from the corresponding author upon reasonable request.

References

1. M. Pardavi-Horvath, Microwave applications of soft ferrites. J. Magn. Magn. Mater. **215–216**, 171–183 (2000). https://doi.org/10.1016/S0304-8853(00)00106-2
2. V.G. Harris, Modern Microwave Ferrites. IEEE Trans. Magn. **48**(3), 1075–1104 (2012). https://doi.org/10.1109/TMAG.2011.2180732
3. S.E. Jacobo, C. Domingo-Pascual, R. Rodriguez-Clemente, M.A. Blesa, Synthesis of ultrafine particles of barium ferrite by chemical coprecipitation. J. Mater. Sci. **32**(4), 1025–1028 (1997). https://doi.org/10.1023/A:1018582423406
4. R.C. Pullar, M.D. Taylor, A.K. Bhattacharya, Novel aqueous sol–gel preparation and characterization of barium M ferrite, $BaFe_{12}O_{19}$ fibres. J. Mater. Sci. **32**(2), 349–352 (1997). https://doi.org/10.1023/A:1018593014378
5. M.A. Almessiere et al., Review on functional bi-component nanocomposites based on hard/soft ferrites: Structural, magnetic, electrical and microwave absorption properties. Nano-Struct. Nano-Obj. **26**, 100728 (2021). https://doi.org/10.1016/j.nanoso.2021.100728
6. Enhancement on the exchange coupling behavior of $SrCo_{0.02}Zr_{0.02}Fe1_{1.96}O_{19}/MFe_2O_4$ (M=Co, Ni, Cu, Mn and Zn) as hard/soft magnetic nanocomposites. https://en.x-mol.com/paper/article/6015309. Accessed 30 Jan 2023
7. M. Zareef Khan, H. Abbas, K. Nadeem, A. Iqbal, I.-L. Papst, Concentration dependent exchange coupling in $BaFe_{12}O_{19}/NiFe_2O_4$ nanocomposites. J. Alloys Compd. **922**, 166105 (2022). https://doi.org/10.1016/j.jallcom.2022.166105

8. S. Manjura Hoque et al., Exchange-spring mechanism of soft and hard ferrite nanocomposites. Mater. Res. Bull. **48**(8), 2871–2877 (2013). https://doi.org/10.1016/j.materresbull.2013.04.009
9. C. Pahwa, S. Mahadevan, S.B. Narang, P. Sharma, Structural, magnetic and microwave properties of exchange coupled and non-exchange coupled $BaFe_{12}O_{19}/NiFe_2O_4$ nanocomposites. J. Alloy. Compd. **725**, 1175–1181 (2017). https://doi.org/10.1016/j.jallcom.2017.07.220
10. H. Yang, M. Liu, Y. Lin, Y. Yang, Simultaneous enhancements of remanence and (BH)max in $BaFe_{12}O_{19}/CoFe_2O_4$ nanocomposite powders. J. Alloy. Compd. **631**, 335–339 (2015). https://doi.org/10.1016/j.jallcom.2015.01.012
11. F. Li, Q. Yang, D.G. Evans, X. Duan, Synthesis of magnetic nanocomposite $MgO/MgFe_2O_4$ from Mg-Fe layered double hydroxides precursors. J. Mater. Sci. **40**(8), 1917–1922 (2005). https://doi.org/10.1007/s10853-005-1211-9
12. K. Ali, J. Iqbal, T. Jana, N. Ahmad, I. Ahmad, D. Wan, Enhancement of microwaves absorption properties of CuFe2O4 magnetic nanoparticles embedded in MgO matrix. J. Alloy. Compd. **696**, 711–717 (2017). https://doi.org/10.1016/j.jallcom.2016.10.220
13. H. Helmiyati, G.H. Abbas, Y. Budiman, S. Ramadhani, Synthesis of $MgFe_2O_4$-MgO nanocomposite: influence of MgO on the catalytic activity of magnesium ferrite in biodiesel production. Rasayan J. Chem. J. Chem. **13**, 298–305 (2020). https://doi.org/10.31788/RJC.2020.1315497
14. R.S. Yadav et al., Magnetic properties of $Co_{1-x}Zn_xFe_2O_4$ spinel ferrite nanoparticles synthesized by starch-assisted sol–gel auto-combustion method and its ball milling. J. Magn. Magn. Mater. **378**, 190–199 (2015). https://doi.org/10.1016/j.jmmm.2014.11.027
15. A. Amri, Z.T. Jiang, T. Pryor, C.-Y. Yin, S. Djordjevic, Developments in the synthesis of flat plate solar selective absorber materials via sol–gel methods: a review. Renew. Sustain. Energy Rev. **36**, 316–328 (2014). https://doi.org/10.1016/j.rser.2014.04.062
16. A. Hajalilou, S.A. Mazlan, K. Shameli, A comparative study of different concentrations of pure Zn powder effects on synthesis, structure, magnetic and microwave-absorbing properties in mechanically-alloyed Ni–Zn ferrite. J. Phys. Chem. Solids **96–97**, 49–59 (2016). https://doi.org/10.1016/j.jpcs.2016.05.001
17. R. Yensano, S. Phokha, Effect of pH on single phase $BaFe_{12}O_{19}$ nanoparticles and their improved magnetic properties. J. Mater. Sci. Mater. Electron. **31**(14), 11764–11773 (2020). https://doi.org/10.1007/s10854-020-03728-6
18. W. Wang, X. Qiao, J. Chen, F. Tan, H. Li, Influence of titanium doping on the structure and morphology of MgO prepared by coprecipitation method. Mater. Char. **60**(8), 858–862 (2009). https://doi.org/10.1016/j.matchar.2009.02.002
19. K. Habanjar, H. Shehabi, A.M. Abdallah, R. Awad, Effect of calcination temperature and cobalt addition on structural, optical and magnetic properties of barium hexaferrite $BaFe_{12}O_{19}$ nanoparticles. Appl. Phys. A **126**(6), 402 (2020). https://doi.org/10.1007/s00339-020-03497-3
20. K. Kumar, A. Loganathan, Structural, electrical and magnetic properties of large ionic size Sr^{2+} ions substituted Mg-Ferrite nanoparticles. Mater. Chem. Phys. **214**, 229–238 (2018). https://doi.org/10.1016/j.matchemphys.2018.04.067
21. A. Azhari, S.M. Sharif, F. Golestanifard, A. Saberi, Phase evolution in Fe_2O_3/MgO nanocomposite prepared via a simple precipitation method. Mater. Chem. Phys. **124**(1), 658–663 (2010). https://doi.org/10.1016/j.matchemphys.2010.07.030
22. S. Kundu, B. Satpati, T. Kar, S.K. Pradhan, Microstructure characterization of hydrothermally synthesized $PANI/V_2O_5{\cdot}nH_2O$ heterojunction photocatalyst for visible light induced photodegradation of organic pollutants and non-absorbing colorless molecules. J. Hazard. Mater. **339**, 161–173 (2017). https://doi.org/10.1016/j.jhazmat.2017.06.034
23. M. Yassine, N. El Ghouch, A.M. Abdallah, K. Habanjar, R. Awad, Structure and magnetic investigation of hard/soft $Ba_{0.5}Sr_{0.5}Fe_{12}O_{19}/x(Ni_{0.5}Zn_{0.5})Fe_2O_4$ nanocomposite. J. Alloy. Compd. **907**, 164501 (2022). https://doi.org/10.1016/j.jallcom.2022.164501
24. R.S. Alam, M. Moradi, M. Rostami, H. Nikmanesh, R. Moayedi, Y. Bai, Structural, magnetic and microwave absorption properties of doped Ba-hexaferrite nanoparticles synthesized by co-precipitation method. J. Magn. Magn. Mater. **381**, 1–9 (2015). https://doi.org/10.1016/j.jmmm.2014.12.059
25. W. Qin, T. Nagase, Y. Umakoshi, J.A. Szpunar, Relationship between microstrain and lattice parameter change in nanocrystalline materials. Philos. Mag. Lett. **88**(3), 169–179 (2008). https://doi.org/10.1080/09500830701840155
26. T. Kaur, S. Kumar, B.H. Bhat, A.K. Srivastava, Enhancement in physical properties of barium hexaferrite with substitution. J. Mater. Res. **30**(18), 2753–2762 (2015). https://doi.org/10.1557/jmr.2015.244
27. H. Shang, J. Wang, Q. Liu, Synthesis and characterization of nanocrystalline $BaFe_{12}O_{19}$ obtained by using glucose as a fuel. Mater. Sci. Eng. A **456**(1), 130–132 (2007). https://doi.org/10.1016/j.msea.2006.12.011
28. S. Vadivelan, N. Victor Jaya, Investigation of magnetic and structural properties of copper substituted barium ferrite powder particles via co-precipitation method. Res. Phys. **6**, 843–850 (2016). https://doi.org/10.1016/j.rinp.2016.07.013
29. G. Kandregula, Structural properties of MgO nanoparticles: synthesized by co-precipitation technique. Int. J. Sci. Res. (IJSR) **3**, 43–46 (2014)
30. J. Wang, Y. Wu, Y. Zhu, P. Wang, Formation of rod-shaped $BaFe_{12}O_{19}$ nanoparticles with well magnetic properties. Mater. Lett. **61**(7), 1522–1525 (2007). https://doi.org/10.1016/j.matlet.2006.07.183
31. I. Altman, I. Agranovski, M. Choi, On nanoparticle surface growth: MgO nanoparticle formation during a Mg particle combustion. Appl. Phys. Lett. **84**, 5130–5132 (2004). https://doi.org/10.1063/1.1764937
32. I.Y. Younis, S.S. El-Hawary, O.A. Eldahshan, M.M. Abdel-Aziz, Z.Y. Ali, Green synthesis of magnesium nanoparticles mediated from Rosa floribunda charisma extract and its antioxidant, antiaging and antibiofilm activities. Sci. Rep. **11**, 16868 (2021). https://doi.org/10.1038/s41598-021-96377-6
33. V. Šepelák et al., The mechanically induced structural disorder in barium hexaferrite, $BaFe_{12}O_{19}$, and its impact on magnetism. Faraday Discuss. **170**, 121–135 (2014). https://doi.org/10.1039/C3FD00137G
34. S. Liu, P. Gao, H. Zou, B. Qin, J. He, L. Deng, Large magnetoelectric effect in $BaFe_{12}O_{19}$-$(Ba_{0.85}Ca_{0.15})(Zr_{0.1}Ti_{0.9})O_3$ particulate composite. Adv. Powder Mater. **1**(3), 100022 (2022). https://doi.org/10.1016/j.apmate.2021.12.001
35. R.S. Azis et al., Effect of ratio in ammonium nitrate on the structural, microstructural, magnetic, and AC conductivity properties of BaFe12O19. Materials (Basel) **11**(11), 2190 (2018). https://doi.org/10.3390/ma11112190
36. S. Maensiri, M. Sangmanee, A. Wiengmoon, Magnesium ferrite ($MgFe_2O_4$) nanostructures fabricated by electrospinning. Nanoscale Res. Lett. (2009). https://doi.org/10.1007/s11671-008-9229-y
37. P. Sharma, A. Kumar, A. Dube, Q. Li, D. Varshney, Structural and dielectric properties of La and Ni-doped M-type $BaFe_{12}O_{19}$ ceramics. AIP Conf. Proc. **1731**(1), 140010 (2016). https://doi.org/10.1063/1.4948176

38. J. Kreisel, G. Lucazeau, H. Vincent, Raman spectra and vibrational analysis of $BaFe_{12}O_{19}$ hexagonal ferrite. J. Solid State Chem. **137**(1), 127–137 (1998). https://doi.org/10.1006/jssc.1997.7737
39. W.Y. Zhao, P. Wei, X.Y. Wu, W. Wang, Q.J. Zhang, Lattice vibration characterization and magnetic properties of M-type barium hexaferrite with excessive iron. J. Appl. Phys. **103**(6), 063902 (2008). https://doi.org/10.1063/1.2884533
40. R. Pandey, L. Kumar Pradhan, S. Kumari, M. Kumar Manglam, S. Kumar, M. Kar, Surface magnetic interactions between $Bi_{0.85}La_{0.15}FeO_3$ and $BaFe_{12}O_{19}$ nanomaterials in $(1-x)$ $Bi_{0.85}La_{0.15}FeO_3$-(x)$BaFe_{12}O_{19}$ nanocomposites. J. Magnet. Magnet. Mater. **508**, 166862 (2020). https://doi.org/10.1016/j.jmmm.2020.166862
41. S. Mallesh, D. Prabu, V. Srinivas, Thermal stability and magnetic properties of $MgFe_2O_4$@ZnO nanoparticles. AIP Adv. **7**(5), 056103 (2017). https://doi.org/10.1063/1.4975355
42. A. Weibel, D. Mesguich, G. Chevallier, E. Flahaut, C. Laurent, Fast and easy preparation of few-layered-graphene/magnesia powders for strong, hard and electrically conducting composites. Carbon **136**, 270–279 (2018). https://doi.org/10.1016/j.carbon.2018.04.085
43. T. Athar, A. Deshmukh, W. Ahmed, Synthesis of MgO nanopowder via non aqueous sol-gel method. Adv. Sci. Lett. **5**, 1–3 (2012). https://doi.org/10.1166/asl.2012.2190
44. P. Dobrosz, S.J. Bull, S.H. Olsen, A.G. O'Neill, "Measurement of the residual macro and microstrain in strained Si/SiGe using Raman spectroscopy. MRS Online Proc. Lib. (OPL) **809**, B3.4 (2004). https://doi.org/10.1557/PROC-809-B3.4
45. R.J. Angel, M. Murri, B. Mihailova, M. Alvaro, Stress, strain and Raman shifts. Z. Kristallogr. Crystall. Mater. **234**(2), 129–140 (2019). https://doi.org/10.1515/zkri-2018-2112
46. F. Naaz, H. Dubey, C. Kumari, P. Lahiri, Structural and magnetic properties of $MgFe_2O_4$ nanopowder synthesized via co-precipitation route. SN Appl. Sci. (2020). https://doi.org/10.1007/s42452-020-2611-9
47. P.J. Burke, Z. Bayindir, G.J. Kipouros, X-ray photoelectron spectroscopy (XPS) investigation of the surface film on magnesium powders. Appl. Spectrosc. **66**(5), 510–518 (2012). https://doi.org/10.1366/11-06372
48. B.C. Brightlin, S. Balamurugan, The effect of post annealing treatment on the citrate sol–gel derived nanocrystalline $BaFe_{12}O_{19}$ powder: structural, morphological, optical and magnetic properties. Appl. Nanosci. **6**(8), 1199–1210 (2016). https://doi.org/10.1007/s13204-016-0531-1
49. F. Mirza, H. Makwana, Synthesis and characterization of magnesium oxide (MgO) nanoparticles by co-precipitation method, **8**(6), 7
50. A. Rodrigues, S. Bauer, T. Baumbach, Effect of post-annealing on the chemical state and crystalline structure of PLD $Ba_{0.5}Sr_{0.5}TiO_3$ films analyzed by combined synchrotron X-ray diffraction and X-ray photoelectron spectroscopy. Ceram. Int. **44**(13), 16017–16024 (2018). https://doi.org/10.1016/j.ceramint.2018.06.038
51. F. Alema, K. Pokhodnya, Dielectric properties of $BaMg_{1/3}Nb_{2/3}O_3$ doped $Ba_{0.45}Sr_{0.55}TiO_3$ thin films for tunable microwave applications. J. Adv. Dielect. **5**(4), 1550030 (2015). https://doi.org/10.1142/S2010135X15500307
52. R. Perez-Gonzalez et al., Highly efficient flexible CNT based supercapacitors fabricated with magnetic $BaFe_{12}O_{19}$ nanoparticles and biodegradable components. J. Phys. Chem. Solids **155**, 110115 (2021). https://doi.org/10.1016/j.jpcs.2021.110115
53. X. Zhang, Y. Zhang, Z. Yue, J. Zhang, Influences of sintering atmosphere on the magnetic and electrical properties of barium hexaferrites. AIP Adv. **9**(8), 085129 (2019). https://doi.org/10.1063/1.5111422
54. Q. Li et al., Vacancy-engineered Gd3+-substituted yttrium iron garnet with narrow ferrimagnetic linewidth and high Curie temperature. J. Alloy. Compd. **935**, 168169 (2023). https://doi.org/10.1016/j.jallcom.2022.168169
55. C. Liu, Y. Zhang, J. Jia, Q. Sui, N. Ma, P. Du, Multi-susceptibile single-phased ceramics with both considerable magnetic and dielectric properties by selectively doping. Sci. Rep. (2015). https://doi.org/10.1038/srep09498
56. H. Cui, X. Wu, Y. Chen, J. Zhang, R.I. Boughton, Influence of copper doping on chlorine adsorption and antibacterial behavior of MgO prepared by co-precipitation method. Mater. Res. Bull. **61**, 511–518 (2015). https://doi.org/10.1016/j.materresbull.2014.10.067
57. K.S. Sánchez-Zambrano et al., XPS study on calcining mixtures of brucite with Titania. Materials (Basel) **15**(9), 3117 (2022). https://doi.org/10.3390/ma15093117
58. J. Lu, X. Wei, Y. Chang, S. Tian, Y. Xiong, Role of Mg in mesoporous $MgFe_2O_4$ for efficient catalytic ozonation of Acid Orange II. J. Chem. Technol. Biotechnol. **91**(4), 985–993 (2016). https://doi.org/10.1002/jctb.4667
59. A.A. Bezlepkin, S.P. Kuntsevich, Domain structure of hexaferrite $BaFe_{12}O_{19}$ near the Curie temperature. Phys. Solid State **62**(7), 1179–1182 (2020). https://doi.org/10.1134/S1063783420070045
60. K. Tanwar, D.S. Gyan, P. Gupta, S. Pandey, D. Kumar, Investigation of crystal structure, microstructure and low temperature magnetic behavior of Ce^{4+} and Zn^{2+} co-doped barium hexaferrites ($BaFe_{12}O_{19}$). RSC Adv. **8**(35), 19600–19609 (2018). https://doi.org/10.1039/C8RA02455C
61. V. Babu, P. Padaikathan, Structure and hard magnetic properties of barium hexaferrite with and without La_2O_3 prepared by ball milling. J. Magn. Magn. Mater. **241**(1), 85–88 (2002). https://doi.org/10.1016/S0304-8853(01)00811-3
62. S.N. Attyabi, S.A. Seyyed Ebrahimi, Z. Lalegani, B. Hamawandi, Reverse magnetization behavior investigation of Mn-Al-C-(α-Fe) nanocomposite alloys with different α-Fe content using first-order reversal curves analysis. Nanomaterials (2022). https://doi.org/10.3390/nano12193303
63. M.K. Manglam, J. Mallick, S. Kumari, R. Pandey, M. Kar, Crystal structure and magnetic properties study on barium hexaferrite (BHF) and cobalt zinc ferrite (CZF) in composites. Solid State Sci. **113**, 106529 (2021). https://doi.org/10.1016/j.solidstatesciences.2020.106529
64. N.A. Algarou et al., Magnetic and microwave properties of $SrFe_12O_{19}/MCe_{0.04}Fe_{1.96}O_4$ (M = Cu, Ni, Mn, Co and Zn) hard/soft nanocomposites. J. Market. Res. **9**(3), 5858–5870 (2020). https://doi.org/10.1016/j.jmrt.2020.03.113
65. Y. Lin, P. Kang, H. Yang, M. Liu, Preparation and characterization of $BaFe_{12}O_{19}/Y_3Fe_5O_{12}$ composites. J. Alloy. Compd. **641**, 223–227 (2015). https://doi.org/10.1016/j.jallcom.2015.03.265
66. X. Shen, F. Song, J. Xiang, M. Liu, Y. Zhu, Y. Wang, Shape anisotropy, exchange-coupling interaction and microwave absorption of hard/soft nanocomposite ferrite microfibers. J. Am. Ceram. Soc. **95**(12), 3863–3870 (2012). https://doi.org/10.1111/j.1551-2916.2012.05375.x
67. M.K. Manglam, S. Kumari, S. Guha, S. Datta, M. Kar, Study of magnetic interaction between hard and soft magnetic ferrite in the nanocomposite. AIP Conf. Proc. **2220**(1), 110020 (2020). https://doi.org/10.1063/5.0001220
68. S. Datta, M.K. Manglam, S.K. Panda, A. Shukla, M. Kar, Investigation of crystal structure and magnetic properties in magnetic composite of soft magnetic alloy and hard magnetic ferrite. Phys. B **653**, 414675 (2023). https://doi.org/10.1016/j.physb.2023.414675
69. M.S. Seehra, S. Suri, V. Singh, Effects of Cu doping on the magnetism of CeO_2 nanoparticles. J. Appl. Phys. **111**(7), 07B516 (2012). https://doi.org/10.1063/1.3676223

70. M.A. Almessiere, Y. Slimani, A. Baykal, Structural and magnetic properties of Ce-doped strontium hexaferrite. Ceram. Int. **44**(8), 9000–9008 (2018). https://doi.org/10.1016/j.ceramint.2018.02.101
71. V.N. Dhage, M.L. Mane, M.K. Babrekar, C.M. Kale, K.M. Jadhav, Influence of chromium substitution on structural and magnetic properties of $BaFe_{12}O_{19}$ powder prepared by sol–gel auto combustion method. J. Alloy. Compd. **509**(12), 4394–4398 (2011). https://doi.org/10.1016/j.jallcom.2011.01.040
72. Z. Mosleh, P. Kameli, M. Ranjbar, H. Salamati, Effect of annealing temperature on structural and magnetic properties of $BaFe_{12}O_{19}$ hexaferrite nanoparticles. Ceram. Int. **40**(5), 7279–7284 (2014). https://doi.org/10.1016/j.ceramint.2013.12.068
73. P. Xu, X. Han, M. Wang, Synthesis and magnetic properties of $BaFe_{12}O_{19}$ hexaferrite nanoparticles by a reverse microemulsion technique. J. Phys. Chem. C **111**(16), 5866–5870 (2007). https://doi.org/10.1021/jp068955c
74. N. Cordente, M. Respaud, F. Senocq, M.-J. Casanove, C. Amiens, B. Chaudret, Synthesis and magnetic properties of nickel nanorods. Nano Lett. **1**(10), 565–568 (2001). https://doi.org/10.1021/nl0100522
75. S. Phokha, J. Klinkaewnarong, S. Hunpratub, K. Boonserm, E. Swatsitang, S. Maensiri, Ferromagnetism in Fe-doped MgO nanoparticles. J. Mater. Sci. Mater. Electron. **27**(1), 33–39 (2016). https://doi.org/10.1007/s10854-015-3713-9
76. S. Azzaza et al., Structural, optical and magnetic characterizations of Mn-doped MgO nanoparticles. Mater. Chem. Phys. **143**(3), 1500–1507 (2014). https://doi.org/10.1016/j.matchemphys.2013.12.006
77. A. Almontasser, A. Parveen, Probing the effect of Ni, Co and Fe doping concentrations on the antibacterial behaviors of MgO nanoparticles. Sci. Rep. (2022). https://doi.org/10.1038/s41598-022-12081-z
78. N. Pathak et al., Defect induced ferromagnetism in MgO and its exceptional enhancement upon thermal annealing: a case of transformation of various defect states. Phys. Chem. Chem. Phys. **19**(19), 11975–11989 (2017). https://doi.org/10.1039/C7CP01776F
79. N. Kumar, D. Sanyal, A. Sundaresan, Defect induced ferromagnetism in MgO nanoparticles studied by optical and positron annihilation spectroscopy. Chem. Phys. Lett. **477**, 360–364 (2009). https://doi.org/10.1016/j.cplett.2009.07.037
80. F. Gao et al., First-principles study of magnetism driven by intrinsic defects in MgO. Solid State Commun. **149**(21), 855–858 (2009). https://doi.org/10.1016/j.ssc.2009.03.010
81. R.D. Widodo, A. Manaf, Physical characteristics and magnetic properties of $BaFe_{12}O_{19}/SrTiO_3$ based composites derived from mechanical alloying. AIP Conf. Proc. **1725**(1), 020098 (2016). https://doi.org/10.1063/1.4945552
82. L. Cao, Z. Wang, Z. Ye, Y. Zhang, L. Zhao, Y. Zeng, Interface exchange coupling induced enhancements in coercivity and maximal magnetic energy product of $BaFe_{12}O_{19}/Co_3O_4$ nanocomposites. J. Alloy. Compd. **715**, 199–205 (2017). https://doi.org/10.1016/j.jallcom.2017.04.284
83. J. Sung Lee, J. Myung Cha, H. Young Yoon, J.-K. Lee, Y. Keun Kim, Magnetic multi-granule nanoclusters: a model system that exhibits universal size effect of magnetic coercivity. Sci. Rep. (2015). https://doi.org/10.1038/srep12135
84. E. Suharyadi, A. Hermawan, D.L. Puspitarum, Crystal structure and magnetic properties of magnesium ferrite ($MgFe_2O_4$) nanoparticles synthesized by coprecipitation method. J. Phys. Conf. Ser. **1091**(1), 012003 (2018). https://doi.org/10.1088/1742-6596/1091/1/012003
85. N. Alghamdi et al., Structural, magnetic and toxicity studies of ferrite particles employed as contrast agents for magnetic resonance imaging thermometry. J. Magn. Magn. Mater. **497**, 165981 (2020). https://doi.org/10.1016/j.jmmm.2019.165981
86. Y. Yang, D. Huang, F. Wang, J. Shao, An investigation on microstructural, spectral and magnetic properties of Pr–Cu double-substituted M-type Ba–Sr hexaferrites. Chin. J. Phys. **57**, 250–260 (2019). https://doi.org/10.1016/j.cjph.2018.11.012
87. F. Fattouh et al., Structural and magnetic properties of hard-soft $BaFe_{12}O_{19}/(Zn_{0.5}Co_{0.5})Fe_2O_4$ ferrites. J. Phys. Condens. Matter (2021). https://doi.org/10.1088/1361-648X/abf478